

Ion adsorption and diffusion in smectite: molecular, pore, and continuum scale views

Ruth M. Tinnacher, Michael Holmboe, Christophe Tournassat, Ian C. Bourg, James A. Davis

▶ **To cite this version:**

Ruth M. Tinnacher, Michael Holmboe, Christophe Tournassat, Ian C. Bourg, James A. Davis. Ion adsorption and diffusion in smectite: molecular, pore, and continuum scale views. Geochimica et Cosmochimica Acta, 2016, 177, pp.130-149. 10.1016/j.gca.2015.12.010 . hal-01368176

HAL Id: hal-01368176
https://brgm.hal.science/hal-01368176

Submitted on 6 Dec 2022

HAL is a multi-disciplinary open access archive for the deposit and dissemination of scientific research documents, whether they are published or not. The documents may come from teaching and research institutions in France or abroad, or from public or private research centers.

L'archive ouverte pluridisciplinaire **HAL**, est destinée au dépôt et à la diffusion de documents scientifiques de niveau recherche, publiés ou non, émanant des établissements d'enseignement et de recherche français ou étrangers, des laboratoires publics ou privés.

Available online at www.sciencedirect.com

ScienceDirect

Geochimica et Cosmochimica Acta 177 (2016) 130–149

Geochimica et Cosmochimica Acta

www.elsevier.com/locate/gca

Ion adsorption and diffusion in smectite: Molecular, pore, and continuum scale views

Ruth M. Tinnacher [a,*], Michael Holmboe [a,b], Christophe Tournassat [a,c], Ian C. Bourg [a,d], James A. Davis [a]

[a] Earth and Environmental Sciences Area, Lawrence Berkeley National Laboratory, Berkeley, CA 94720, United States
[b] Department of Chemistry, Umeå University, Uppsala, Sweden
[c] BRGM, French Geological Survey, Orléans, France
[d] Department of Civil and Environmental Engineering (CEE) and Princeton Environmental Institute (PEI), Princeton University, Princeton, NJ 08544, United States

Received 3 April 2015; accepted in revised form 11 December 2015; available online 17 December 2015

Abstract

Clay-rich media have been proposed as engineered barrier materials or host rocks for high level radioactive waste repositories in several countries. Hence, a detailed understanding of adsorption and diffusion in these materials is needed, not only for radioactive contaminants, but also for predominant earth metals, which can affect radionuclide speciation and diffusion. The prediction of adsorption and diffusion in clay-rich media, however, is complicated by the similarity between the width of clay nanopores and the thickness of the electrical double layer (EDL) at charged clay mineral–water interfaces. Because of this similarity, the distinction between 'bulk liquid' water and 'surface' water (i.e., EDL water) in clayey media can be ambiguous. Hence, the goal of this study was to examine the ability of existing pore scale conceptual models (single porosity models) to link molecular and macroscopic scale data on adsorption and diffusion in compacted smectite. Macroscopic scale measurements of the adsorption and diffusion of calcium, bromide, and tritiated water in Na-montmorillonite were modeled using a multi-component reactive transport approach while testing a variety of conceptual models of pore scale properties (adsorption and diffusion in individual pores). Molecular dynamics (MD) simulations were carried out under conditions similar to those of our macroscopic scale diffusion experiments to help constrain the pore scale models. Our results indicate that single porosity models cannot be simultaneously consistent with our MD simulation results and our macroscopic scale diffusion data. A dual porosity model, which allows for the existence of a significant fraction of bulk liquid water—even at conditions where the average pore width is only a few nanometers—may be required to describe both pore scale and macroscopic scale data.
© 2016 Elsevier Ltd. All rights reserved.

1. INTRODUCTION

Nuclear fission produces 14% of the world's electricity supply and could contribute ~15% of CO_2 abatement efforts required to stabilize global CO_2 emissions over the next 50 years (Pacala and Socolow, 2004; Englert et al., 2012). The viability of nuclear energy as a CO_2 abatement technology, however, relies in part on the demonstration that geologic storage facilities can isolate high level radioactive waste (HLRW) on time scales commensurate with the decay of long-lived radioactive fission products, on the order of 10^6 years. Accurate predictions of repository performance on such long time scales require the development

* Corresponding author. Tel.: +1 (510) 495 8231; fax: +1 (510) 486 5686.
E-mail address: RMTinnacher@lbl.gov (R.M. Tinnacher).

http://dx.doi.org/10.1016/j.gca.2015.12.010
0016-7037/© 2016 Elsevier Ltd. All rights reserved.

Notation

A	cross-sectional area available for diffusion (m^2)
a_s	specific surface area of the material ($m^2\ g^{-1}$)
C_b	species concentration in bulk pore water (mol dm^{-3})
$C_{i,bulk}$	species concentration in bulk pore water (mol dm^{-3})
$C_{i,EDL}$	species concentration in diffuse layer (mol dm^{-3})
$C_{i,free}$	species concentration in 'free' water (mol dm^{-3})
$C_{i,midplane}$	species concentration at the interlayer midplane (mol dm^{-3})
$C_{i,pore}$	average species concentration in the entire nanopore (mol dm^{-3})
C_{low}	solute concentration in low-concentration reservoir at time t (mol dm^{-3})
C_{high}	solute concentration in high-concentration reservoir at time t (mol dm^{-3})
d_D	mean electric double layer thickness (Å)
d_{pore}^{hom}	average pore thickness (nm)
D_0	self-diffusion coefficient in bulk liquid water ($m^2\ s^{-1}$)
D_a	apparent diffusion coefficient ($m^2\ s^{-1}$)
D_e	effective diffusion coefficient ($m^2\ s^{-1}$)
D_p	pore diffusion coefficient in macroscopic models ($m^2\ s^{-1}$)
D_{pore}	two-dimensional diffusion coefficient in MD simulations ($m^2\ s^{-1}$)
D_s	surface diffusion coefficient ($m^2\ s^{-1}$)
f	'free' water fraction of porosity (–)
F	Faraday's constant (96490 C mol^{-1})
G	geometric factor (–)
G_f	geometric factor for metal filters (–)
h_{pore}	average pore width (nm)
J	solute mass density in x direction (e.g., mol $s^{-1}\ m^{-2}$)
J_N	normalized diffusive flux (m day^{-1})
K_{Ca}	calcium surface complexation constant
K_D	adsorption coefficient (cm^{-3} g or dm^{-3} kg)
K_{Na}	sodium surface complexation constant (cm^{-3} g or dm^{-3} kg)
$\langle l^2 \rangle$	mean-square displacement of species as a function of time
m_i	adsorbed solute per mass of clay (mol kg^{-1})
M	mass of clay per volume of pore water (kg dm^{-1})
q_{nano}	parameter accounting for slow diffusion in vicinity of clay mineral surfaces (–)
R	molar gas constant (8.314 J $mol^{-1}\ K^{-1}$)
t	time (s or day)
T	temperature (K)
V_{low}	volume of low-concentration reservoir at time t (cm^{-3})
x	distance (m)
z_i	ionic charge (–)
α	rock capacity factor (–)
Δt	time interval between low-conc. reservoir solution replacements (day)
θ	total porosity of clay (–)
θ_e	effective or anion-accessible porosity (–)
θ_f	porosity of metal filters (–)
v_{DIS}	ratio of diffusion coefficients in bulk liquid water and DIS water (–)
ρ_b	dry bulk density (g cm^{-3})
ρ_{dry}	dry density (g cm^{-3})
ρ_g	crystal or grain density (g cm^{-3})
σ_0	surface charge (C m^{-2})
σ_D	surface charge compensated in diffuse layer (C m^{-2})
τ	time (ps)
ϕ	porosity (–)
ϕ_e	effective porosity accounting for anion exclusion (–)
ψ	surface potential (V)
ψ_{DIS}	mean electrostatic potential in the diffuse layer (V)
$\psi_{midplane}$	electrostatic potential at the midplane of the nanopore (V)

of geophysical models grounded in fundamental knowledge of material properties and constitutive relationships relevant to radionuclide migration in geologic media (Altmann et al., 2012).

Most countries with HLRW storage programs are currently investigating clayey media, such as bentonite and shale, for use as engineered barriers and/or host rocks of geologic repositories (Andra, 2005; Delay et al., 2007; Altmann, 2008; Guyonnet et al., 2009; Bock et al., 2010; SKB, 2011; Altmann et al., 2012). At the conditions that would exist in proposed HLRW repositories, clay barriers display very low hydraulic conductivities, the ability to self-heal when fractured, and water and solute mass fluxes that are dominated by molecular diffusion on time-scales of millions of years (Neuzil, 1986, 1994, 2013; Horseman and Volckaert, 1996; Oscarson et al., 1996; Bock et al., 2010; Mazurek et al., 2011). The diffusion coefficients of water and solutes in clayey media have been extensively studied in conditions relevant to HLRW repositories, particularly in the case of water tracers (HTO), anions (I^-, Br^-, Cl^-, TcO_4^-, SeO_3^{2-}), and alkali and alkaline earth metals (Na^+, Cs^+, Ca^{2+}, Sr^{2+}) (Appelo et al., 2010; Savoye et al., 2010, 2011; Gimmi and Kosakowski, 2011; Holmboe et al., 2011; Loomer et al., 2013; Tachi and Yotsuji, 2014; Bourg and Tournassat, 2015). It is important to note that an understanding of diffusion rates is needed for both relevant radionuclides and predominant earth metals, because the latter elements can affect actinide solution speciation and compete with radionuclides for mineral surface sites. For instance, within engineered clay barriers

containing minor amounts of calcite, $Ca_2UO_2(CO_3)_3^0$ is expected to dominate uranium(VI) solution speciation, and hence, control U(VI) sorption and diffusion behavior (Kerisit and Liu, 2010; Bradbury and Baeyens, 2011; Joseph et al., 2011).

Sodium-montmorillonite is the main constituent of bentonite, the engineered barrier material considered for use in HLRW repositories in many countries (Nadeau, 1985; Zachara and Smith, 1994; Sposito et al., 1999; Tournassat et al., 2003; Yokoyama et al., 2005). Montmorillonite is a smectite, a 2:1-layer-type dioctahedral phyllosilicate with a large specific surface area ($\sim$800 $m^2\ g^{-1}$) and cation exchange capacity ($\sim$1 $mmol_c\ g^{-1}$), each clay mineral layer having a thickness of $\sim$1 nm and carrying negatively-charged isomorphic substitutions in its phyllosilicate framework. The aggregation of Na-montmorillonite layers into particles (i.e., stacks of clay mineral layers) results in a complex pore-size distribution including narrow ($\sim$1 nm wide) interlayer pores within particles (where diffusion is strongly impacted by clay mineral surfaces) and larger pores between particles (where water may be bulk-liquid-like).

Diffusion of dilute conservative solutes in porous media can be described using an effective diffusion coefficient D_e defined by the following Fickian expression:

$$J = -D_e \frac{\partial C_b}{\partial x} \tag{1}$$

where J is the solute mass flux density in the x direction and C_b is the concentration of the species of interest in bulk pore water. (Units for all variables are provided in the Notation section.) If adsorption is linear and instantaneous, Eq. (1) can be combined with a local mass balance relation to obtain the expression:

$$\alpha \frac{\partial C_b}{\partial t} = \frac{\partial}{\partial x}\left[D_e \frac{\partial C_b}{\partial x}\right] \tag{2}$$

where the rock capacity factor α depends on porosity θ, the dry bulk density of the porous medium ρ_b, and the slope of the linear sorption isotherm K_D according to the relation:

$$\alpha = \theta + \rho_b K_D \tag{3}$$

In macroporous media, D_e depends only on θ, a geometric factor G ($\geqslant 1$) that describes the influence of pore-network geometry [i.e., the orientation, shape, and connectivity of pores (Bear, 1972; Dykhuizen and Casey, 1989; Shackelford and Moore, 2013)], and the self-diffusion coefficient of the species of interest in bulk liquid water D_0:

$$D_e = \frac{\theta}{G} D_0 \tag{4}$$

In clayey media, however, Eq. (4) overestimates the diffusion of anions and underestimates the diffusion of cations (Molera et al., 2003; Appelo et al., 2010; Gimmi and Kosakowski, 2011). This discrepancy arises from the fact that a significant fraction of pore water is located in the electrical double layer (EDL), the interfacial water region where cation adsorption and anion exclusion screen the negative clay mineral surface charge. In particular, in clay rocks and smectite barriers considered for use in HLRW storage, most of the pore fluid is located in pores narrower than 10 nm (Holmboe et al., 2012; Keller et al., 2013). For comparison, the characteristic thickness of the EDL is $\sim$2 nm for 1:1 electrolytes with concentrations of 0.1 M according to the well-known Gouy-Chapman theory (Sposito, 1992, 2004). Because of this similarity between pore width and EDL thickness, much of the pore water in smectite-rich media has properties distinct from those of bulk liquid water (Sato, 2008; Mazurek et al., 2011). The distinct properties of clayey media (Laird and Shang, 1997; Jo et al., 2006; Gajo and Loret, 2007) are particularly pronounced in conditions where the characteristic thickness of the EDL is greater than one half of the pore width, such that overlapping EDLs on opposite pore walls occupy the entire pore space.

Despite the extensive database on diffusion in clayey media, a widely accepted alternative to Eq. (4) in these systems has yet to emerge. Overall, the various modeling strategies can be summarized in three, broad categories: (1) semi-empirical approaches, (2) single porosity models and (3) dual porosity models. The first approach consists in modifying Eq. (4) to account for the effect of pore scale couplings by introducing semi-empirical parameters. These parameters account for (a) the slower diffusion dynamics of water and *uncharged solutes* in the vicinity of clay mineral surfaces than in bulk liquid water (Kemper et al., 1964; Bourg et al., 2006; Gonzàlez Sànchez et al., 2009; Churakov and Gimmi, 2011; Holmboe and Bourg, 2014) using the parameter $q_{nano} \leqslant 1$ (Eq. (5)),

$$D_{e,uncharged} = \frac{\theta}{G} q_{nano} D_0 \tag{5}$$

(b) the lower effective or "anion-accessible" porosity ($\theta_e \leqslant \theta$, Eq. (6)) due to *anion* exclusion (negative adsorption) in the EDL (Van Schaik and Kemper, 1966; Mazurek et al., 2011; Shackelford and Moore, 2013),

$$D_{e,anion} = \frac{\theta_e}{G} D_0 \tag{6}$$

and (c) the significant mobility of adsorbed *cations* in the EDL (Jenny and Overstreet, 1939; Van Schaik et al., 1966; Nye, 1980; Jakob et al., 2009; Gimmi and Kosakowski, 2011) based on a surface diffusion coefficient D_s (Eq. (7)).

$$D_{e,cation} = \frac{\theta}{G} D_0 + \rho_b K_D D_s \tag{7}$$

Eqs. (5)–(7) provide convenient phenomenological descriptions of D_e, but their predictive capabilities, inherently, are contingent upon the existence of accurate models for the newly introduced parameters (q_{nano}, θ_e, K_D, and D_s).

A second approach consists in developing conceptual models of adsorption and diffusion in individual, slit-shaped clay nanopores, and then, using these pore scale models to predict macroscopic-scale D_e values in clayey media (Leroy et al., 2006; Birgersson and Karnland, 2009; Jougnot et al., 2009; Appelo et al., 2010; Tachi and Yotsuji, 2014; Tachi et al., 2014). The availability of a large variety of single porosity models (Fig. 1) suggests that existing macroscopic scale data do not strongly constrain

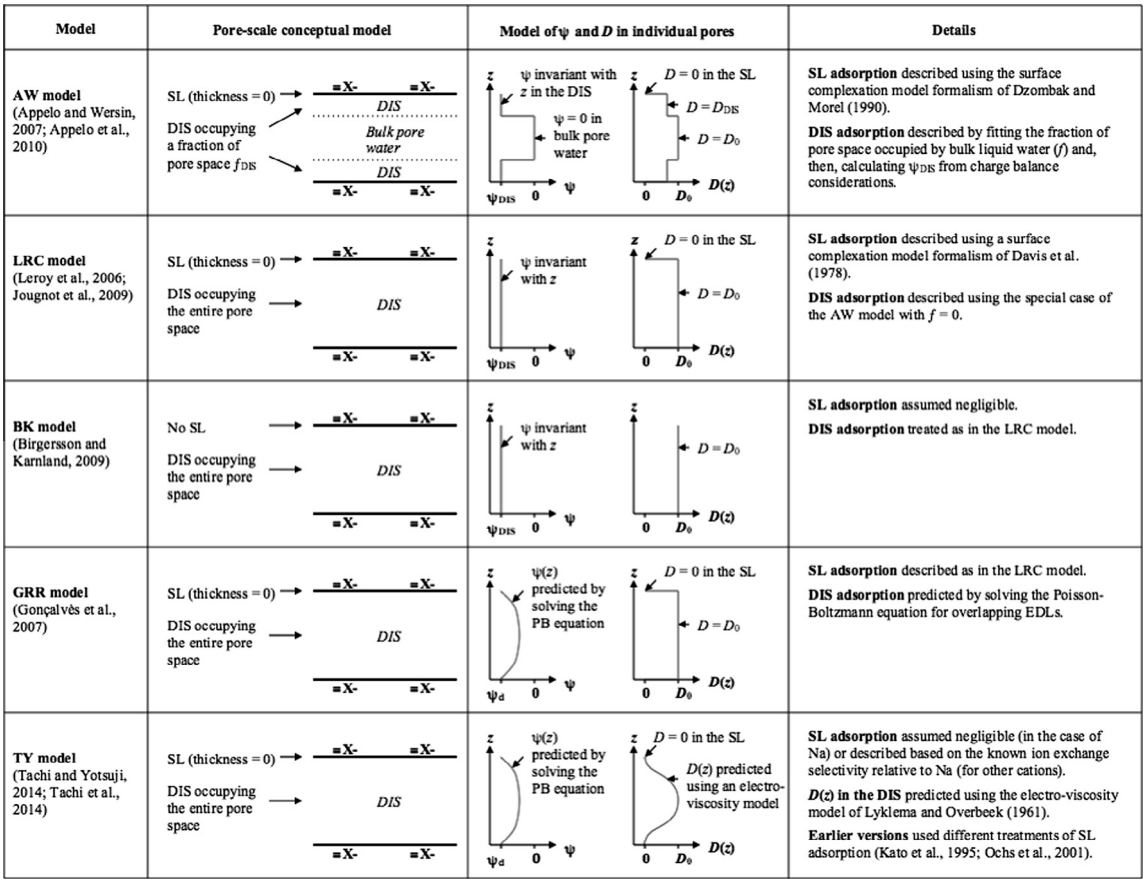


Fig. 1. Overview of pore-scale conceptual models describing diffusion and adsorption processes in clay interlayer spaces as single porosity (AW, LRC, BK, GRR, TY) models. Model names are based on authors of related publications. The electrical double layer (EDL) is almost invariably modeled as the sum of a Stern layer (SL) and a diffuse ion swarm (DIS), the latter being characterized by the electrostatic potential profile across the pore, $\psi(z)$.

all features in these models. In particular, two significant challenges hinder efforts to constrain the pore-scale models summarized in Fig. 1. Firstly, the structure of the EDL in clayey media has never been directly observed: existing models are based on theoretical calculations (Sposito, 1992) or atomistic simulations (Marry et al., 2002, 2008; Tournassat et al., 2009; Bourg and Sposito, 2011). Secondly, the microstructure of water-saturated clayey media is not precisely known in the range of conditions relevant to HLRW repositories (high solid–water ratios, broad range of salinities). As a consequence, these models use the simplifying assumption (explicitly or implicitly) that clayey media are dominated by slit-shaped pores with a pore width h_{pore}, equal to the average pore width in the medium. This simplification obviates the need for information on the microstructure of the medium, because the average pore width can be calculated from the dry bulk density ρ_b and specific surface area a_s of the material. Experimental studies using X-ray diffraction (Ferrage et al., 2005; Holmboe et al., 2012), small angle neutron scattering (Swift et al., 2014), and nuclear magnetic resonance (Montavon et al., 2009), however, show that pore-size distributions in clayey media are often bimodal or more complex, raising questions about the appositeness of the "single pore width" assumption.

A third approach consists in developing models of water and ion diffusion that account for the pore-size distribution in clayey media. Models of this type have been used to describe water and cation diffusion (Bourg et al., 2006; Bourg and Sposito, 2010; Churakov and Gimmi, 2011; Bourg and Tournassat, 2015), anion exclusion (Tournassat and Appelo, 2011), pore water geochemistry (Wersin et al., 2004), and swelling mechanics (Wang et al., 2013). The challenge is that the microstructure of clay barriers is arduous to characterize with sufficient resolution to constrain existing models: X-ray diffraction techniques can detect the smallest pores present in smectite clay barriers (0.3–0.9 nm) and some larger scale features, such as osmotic hydrates and interstratified stacking arrangements, but they are limited with regard to larger-scale stacking arrangements and sensitive to sample preparation techniques (Holmboe et al., 2010, 2012). Electron microscopy techniques are not yet able to probe the microstructure of the smallest pores in compacted clayey media due to beam damage and microstructural changes during sample preparation.

The present situation clearly indicates two research questions: (1) Do single porosity models, summarized in Fig. 1, correctly predict ion density and diffusion profiles across clay nanopores? and (2) Is the use of an average pore width sufficient to describe diffusion in clayey media, or are models accounting for a distribution of pore sizes needed?

In order to answer these questions, we performed a combined experimental and modeling study to examine the consistency of macroscopic adsorption and diffusion measurements, pore scale models, and molecular dynamics (MD) simulations in the case of cations, anions, and uncharged species in a single effort and over multiple scales. First, we present new macroscopic scale measurements of the adsorption and diffusion of trace levels of Ca^{2+}, Br^-, and tritiated water (HTO) in water-saturated Na-exchanged smectite (montmorillonite). The results are then modeled using a multi-component reactive transport approach based on the models described in Fig. 1. Model assumptions and parameters are then tested against new MD simulation results on water and ion adsorption and diffusion in individual clay interlayer nanopores carried out under similar conditions to our laboratory diffusion experiment. These combined results allow us to critically evaluate the underlying assumptions of the models compiled in Fig. 1, and the ability of these models to link the pore scale and macroscopic scale properties of compacted smectite. Our MD simulations are the first, to our knowledge, to examine the competitive adsorption of several cationic and anionic species in the EDL on smectite surfaces under relatively dilute conditions (representative of a pore at equilibrium with a 0.1 M NaCl solution).

2. EXPERIMENTAL AND MODELING METHODS

2.1. Experimental

2.1.1. Clay pretreatment and characterization

A commercially available, well-characterized standardized Source Clay (Na-montmorillonite, SWy-2, The Clay Minerals Society) was selected in order to allow for a subsequent comparison with other data from the literature. The material is known to contain significant amounts of impurities including quartz (8%), feldspars (16%) and calcite (Chipera and Bish, 2001; Costanzo and Guggenheim, 2001; Mermut and Cano, 2001). Prior to its use, the clay was pretreated to remove major mineral impurities while preserving the original clay characteristics as much as possible, following an adaptation of published methods (Jackson, 1975). The complete procedure is described in detail in the Electronic Annex (EA). Briefly, pretreatment steps included: the removal of calcite impurities using a 1 M sodium acetate/glacial acetic acid solution (0.564 M) at pH 5; clay equilibration with a 1 M sodium chloride solution; removal of excess salts with Nanopure water; separation of quartz and feldspar impurities from the <2 μm clay fraction by centrifugation; and oven-drying of the purified clay at 45 °C. This purification procedure allowed us to keep calcium background concentrations at or below 88.1 μg dm^{-3} in the reservoir solutions during the through-diffusion experiment, with a contribution of 33.2 μg dm^{-3} from the background electrolyte itself. All chemicals used in this study were reagent grade or better. Acids, bases, and salt solutions used in experiments were of TraceSelect (Sigma Aldrich) or comparable grade in order to minimize calcium background concentrations.

2.1.2. Calcium bromide through-diffusion experiment

The calcium bromide through-diffusion experiment largely followed procedures previously described in the literature (Molera and Eriksen, 2002; Van Loon et al., 2003a, 2003b). The experimental setup consists of a diffusion cell, high and low concentration reservoirs, and a peristaltic pump (Fig. EA-1, Electronic Annex). All experimental solutions were repeatedly adjusted to pH 7 using small volumes of acid/base solutions (TraceSelect grade NaOH and HCl), while equilibrating with atmospheric CO_2 over 3–6 days, prior to their contact with the mineral phase.

At the beginning of the experiment, dry, pretreated Na-montmorillonite was packed into the diffusion cell (PEEK; $D = 1.0$ cm, $L = 0.5$ cm; Alltech 2 μm stainless-steel frits, P/N 721825) by hand to obtain a dry bulk density of 0.8 $\pm$ 0.03 kg dm^{-3}. This dry density value was selected in order to test a system where both clay macro- and micropore structures may be relevant and to ensure solute breakthrough within reasonable, experimental time-frames. For comparison, dry densities of compacted bentonite in proposed waste repositories are expected at around 1.6 kg dm^{-3}. The clay was carefully compacted with a custom-made PEEK rod and, then, saturated with the background electrolyte (0.1 M NaCl, pH 7) by circulating electrolyte solutions at 0.7 mL min^{-1} for about 4 1/2 weeks.

After clay saturation, the solutions in the high and low concentration reservoirs were replaced by 200 mL of background electrolyte containing 1 mM $CaBr_2$ and a 20 mL aliquot of fresh, $CaBr_2$-free electrolyte, respectively. Over the following weeks, the circulation of solutions was continued at the same flow rate. Electrolyte solutions in the low concentration reservoir were regularly replaced in order to maintain a nearly constant concentration gradient between the high and low concentration reservoirs, with <0.02 mM $CaBr_2$ in the low concentration reservoir at all times. The collected low concentration reservoir vials were weighed to correct for volume losses due to evaporation. Solutions were sampled for Ca and Br analysis by ion chromatography (IC) and flow injection analysis (FIA), respectively (Lachat QuikChem 8500 Series 2 Automated Ion Analyzer, IC Cations: method: #10-520-00-1-D, FIA-Bromide method: #30-135-21-1-A), and their solution pH values were recorded. In addition, small volumes (1.5 mL) of the high concentration reservoir solution were regularly sampled for the monitoring of Ca and Br concentrations and concentration gradients. This procedure was continued until a series of data points had been collected under steady-state Ca and Br diffusion. The solution in the high concentration reservoir was then replaced with a $CaBr_2$-free background electrolyte containing approximately 1000 Bq mL^{-1} (27 nCi mL^{-1}) of tritiated water (HTO). Again, low concentration reservoir solutions were continuously replaced, and tritium activities were analyzed (PerkinElmer Liquid Scintillation Analyzer Tri-Carb 2900TR;

Ultima Gold XR liquid scintillation cocktail) until a sufficient number of data points had been collected under steady-state HTO diffusion.

2.1.3. Determination of anion-accessible porosity

Preliminary modeling results showed a difference between the diffusion-accessible porosity for tritiated water (HTO) and the anion (bromide) in packed Na-montmorillonite. Hence, a "static" experiment was conducted to determine the anion-accessible porosity using the same background electrolyte solution and a similar bromide concentration as in the through-diffusion experiment. In the static experiment, the diffusion cell containing the dry packed clay was directly connected to two 200 mL, high concentration reservoirs (0.1 M NaCl, 0.00085 M NaBr, pH 7) in order to facilitate a faster equilibration of the clay with bromide ions. After equilibration for 33 days, the wet clay was extruded and dried at 150 °C to determine its water content by weight difference and to compute the dry bulk density of the porous medium. Bromide was extracted from the dried and ground mineral phase by leaching (Muurinen et al., 2004, 2007; Van Loon et al., 2007). Briefly, aliquots of approximately 30 mg Na-montmorillonite were transferred into 15-mL centrifuge tubes (four replicates) and 10-mL aliquots of Nanopure water were added. After shaking overhead for three days, the suspensions were centrifuged (Beckman Coulter Avanti J-E, 20 000 *g* for 30 min), and the supernatant solutions were filtered with 0.2 μm membrane filters. The resulting solutions were analyzed for Br by inductively coupled plasma mass spectrometry (ICP-MS) using a Perkin-Elmer SCIEX ICP-Mass Spectrometer ELAN DRC II.

2.2. Multi-component transport modeling

The diffusion experiments were modeled with PHREEQC v3.0 in a 1D geometry using the multi-component diffusion (MCD) capabilities of the code. Details of the system geometry are given in the Electronic Annex (Fig. EA-2). Relevant equations and numerical methods are described in detail elsewhere (Parkhurst and Appelo, 1999, 2013; Appelo and Wersin, 2007; Appelo et al., 2010). Self-diffusion coefficients in bulk liquid water for individual chemical species were taken from the PHREEQC.dat database.

A constant tracer concentration was assigned to the high concentration reservoir. The renewal of the electrolyte solution in the low concentration reservoir with each sampling event has a non-negligible effect on the solute concentration gradients and, thus, on the recorded fluxes (Glaus et al., 2015). This effect was taken into account during the simulation by allowing tracers to accumulate as a function of time in two numerical cells: a first cell representing the low concentration reservoir, and a second cell representing a "dead volume" located between the clay sample and the low concentration reservoir (mimicking the tubing of the peristaltic pump). After each sampling event, the tracer concentration was reset to zero in the numeric cell representing the low concentration reservoir, but not in the cell representing the dead volume. As shown below, this approach allowed us to predict the impact of small variations in the sampling intervals on diffusive mass fluxes.

In the following, the data are presented in terms of diffusive mass fluxes in order to comply with the typical presentation style for diffusion data in the literature. No temperature correction was done. Diffusion in the filters and in the dead volume at the end of the experimental device was explicitly taken into account. Transport parameters for the filters were obtained from the literature (Molera, 2002; Molera et al., 2003) as the same filters were used for the present study: porosity $\theta_f = 0.25$, geometrical factor $G_f = 2.33$, height = 0.79 mm. Molera and co-workers found identical G_f values for Na^+, Cs^+ and Sr^{2+} diffusion; hence, we assumed that the filter diffusion parameters were identical for all chemical species in our experiments.

The modeling strategy was similar to the one developed in Appelo et al. (2010). In the first step, HTO, Br, and Ca diffusion were modeled individually with the simple Fickian model (Eqs. (1) and (2)) in order to derive species-dependent values of α and D_e. In a second step, pore scale models proposed in previous studies (Fig. 1) were tested against our experimental data and compared with our MD simulation results.

2.3. Molecular dynamics simulations

Molecular dynamics (MD) simulations of a Na–Ca–Cl–Br aqueous solution confined in a 31.5 Å wide nanopore between parallel smectite basal surfaces were carried out in conditions that approximate the solid/water ratio and aqueous geochemistry of our adsorption and diffusion experiments. Our simulation methodology is known for accurate predictions of diffusion coefficients and activation energies of diffusion of water and sodium in smectite interlayer nanopores for pore widths ranging from 0.3 to 30 Å and temperatures ranging from 278 to 353 K (Holmboe and Bourg, 2014). In brief, simulations were carried out with the program LAMMPS (Plimpton, 1995) using periodic boundary conditions. Inter-atomic interactions were described with the SPC/E model of liquid water (Berendsen et al., 1987), the CLAYFF model of mineral–water interactions (Cygan et al., 2004), the parameters of Joung and Cheatham (2009) for the alkali and halide ions, and the parameters of Aaqvist (1990) for Ca^{2+}. Water molecules were kept rigid using the SHAKE algorithm (Ryckaert et al., 1977). All clay mineral atoms were kept immobile except for structural H atoms. Production runs from two different initial configurations, differing only by their initial distribution of the interlayer ions, were carried out in the *NVT* ensemble (constant composition, volume, and temperature) with a 1 fs time step for a total duration of 105 ns. The production runs were preceded by 1 ns of equilibration in the *NPT* ensemble (at $P = 1$ bar) and 5 ns of equilibration in the *NVT* ensemble. Comparison of the two production runs allowed us to verify that the equilibrium ion density profiles were not influenced by the initial distribution of the ions. Reported density profiles and diffusion coefficients are average values for the two production runs. Electrostatic and dispersion interactions beyond

12 Å were computed with the particle–particle particle-mesh (PPPM) solver (Hockney and Eastwood, 1988; Isele-Holder et al., 2012). Two-dimensional diffusion coefficients (D_{pore}) in the xy plane of the interlayer nanopores were calculated with the well-known Einstein relation:

$$D_{pore} = \frac{1}{2n} \lim_{\tau \to \infty} \frac{d\langle l^2 \rangle}{d\tau} \quad (8)$$

where $n = 2$ for diffusion in the xy plane and $\langle l^2 \rangle$ is the mean-square displacement of the species of interest as a function of time τ. Three-dimensional diffusion coefficients were not calculated, because the large shape ratio of clay interlayer nanopores (a few nanometers wide in the z direction, but hundreds of nanometers wide in the xy plane) renders diffusion in the z direction essentially irrelevant to the objective of predicting macroscopic-scale diffusion coefficients. The infinite-time limit in the Einstein relation was evaluated using the slope $\langle l^2 \rangle$ vs. τ for $\tau = 150$– 250 ps, as calculations using shorter probe time scales may not accurately reflect the infinite-time diffusive limit in clay interlayers (Bourg and Sposito, 2010; Holmboe and Bourg, 2014).

In order to calculate D_{pore} as a function of distance from the surface, the pore was divided into 0.2 Å thick slices parallel to the clay mineral surfaces. As the average residence time of individual water molecules or ions within each slice was only a fraction of τ, the mean square displacement within each slice was analyzed by applying Eq. (8) to a "mended trajectory" constructed by appending all segments of trajectory data of the species of interest in each slice into a single pseudo-trajectory as described in the Electronic Annex.

The simulated system contained 180 clay mineral unit cells with an average unit cell formula of $Si_8(Al_{3.33}Mg_{0.67})O_{20}(OH)_4$, 116 Na^+ ions, 4 Ca^{2+} ions, 3 Cl^- ions, 1 Br^- ion, and 9000 water molecules (total of 34 324 atoms) in a 93.305 × 90.030 × 40.913 Å simulation cell (Fig. 2). The system was designed to approximate the conditions of the macroscopic diffusion experiment. The average unit cell formula used in our simulations represents a typical Wyoming-type montmorillonite similar to that of the clay used in the experiments (untreated Na-montmorillonite, SWy-2, The Clay Minerals Society: $(Ca_{0.52}Na_{0.14}K_{0.01})[Al_{3.23}Fe(III)_{0.42}Mg_{0.56}][Si_{7.89}Al_{0.11}]O_{20}(OH)_4$, Mermut and Cano, 2001). The dry bulk density in our MD simulations [$\rho_b = 0.65$ - kg dm^{-3}, calculated using a smectite particle thickness of 9.4 Å and a clay mineral layer density of 2.84 kg dm^{-3} (Bourg et al., 2006; Tournassat and Appelo, 2011)] was close to that used in the experiments. The small difference in density between the two systems (experimental diffusion cell and MD simulation cell) is accidental but only reinforces the main finding of our study: the MD simulations overestimate anion exclusion relative to the experiments, and they would overestimate anion exclusion even more strongly if they had been carried out with exactly the same solid–water ratio. The average composition of the nanopore water (0.712 M Na^+, 0.247 M Ca^{2+}, 0.019 M Cl^-, 0.006 M Br^-) was selected to approximate the expected composition in a real pore with the same width and surface charge density in equilibrium with a 0.1 M NaCl bulk aqueous solution with minor concentrations of Ca^{2+} and Br^-, as in our macroscopic scale experiments. The average composition of the nanopore water was estimated using the Poisson–Boltzmann equation, as described in Section 3.3.2.

3. RESULTS

3.1. Experimental results

3.1.1. Diffusion breakthrough curves

Experimental data in tabulated form are provided in the Electronic Annex in order to allow other researchers to conduct their own model simulations of this experiment. Normalized mass flux densities reaching the low concentration reservoir (J_N in m day^{-1}) were calculated with the expression:

$$J_N = \frac{C_{low}}{C_{high}} \frac{V_{low}}{A \cdot \Delta t} \quad (9)$$

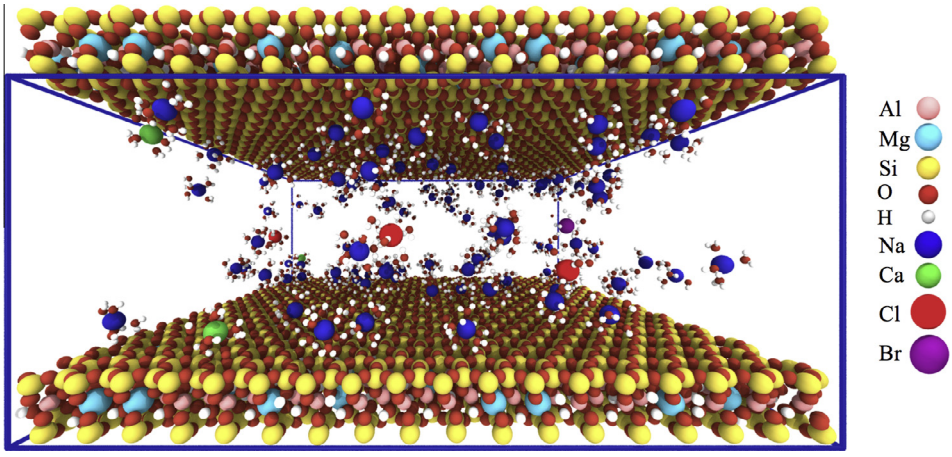


Fig. 2. Snapshot of our MD simulation cell showing the smectite clay layer and the 31.5 Å wide interlayer nanopore containing Na^+ (blue), Ca^{2+} (green), Br^- (purple), and Cl^- (red) ions with their first hydration shell water molecules. Other water molecules are not shown. The clay mineral structure contains Si (yellow), Al (pink), Mg (light blue), O (red), and H (white) atoms.

where C_{low} is the concentration of the species of interest measured in the low concentration reservoir at a sampling event, C_{high} is the constant concentration in the high concentration reservoir, Δt is the time interval since the previous sampling event (in days), A is the cross sectional area of the diffusion cell (0.785 cm^2), and V_{low} is the volume of the low-concentration reservoir (about 20 mL).

The low concentration reservoir solution was replaced frequently during the experiment to ensure that $C_{low}/C_{high} < 0.02$. However, it was not feasible to exchange the low concentration reservoir solution on a perfectly even schedule. Thus, at steady state flux conditions, C_{low} fluctuated significantly from sample to sample, because C_{low} increased with Δt (Fig. 3).

Normalized diffusion fluxes at steady state increased in the order of $J_{Br} < J_{HTO} < J_{Ca}$, i.e., from anion to neutral species to cation. This finding is in agreement with previously reported results. Steady state diffusion was attained after a few days for HTO and Br, and after one month for Ca. A greater retardation of Ca breakthrough is expected based on the adsorption of Ca^{2+} onto smectite clay surfaces.

3.1.2. Total porosity and anion accessible porosity from the static experiment

The clay was compacted to a calculated dry bulk density $\rho_b = 0.79$ kg dm^{-3} based on the mass of clay packed and the volume of the cell. The crystal density of clay mineral layers (or grain density, ρ_g) is about 2.84 kg dm^{-3} (Bourg et al., 2006; Tournassat and Appelo, 2011). If we neglect the small difference between the ρ_g values of clay mineral layers and impurities (mostly fine grained quartz), the porosity of the material is given by:

$$\theta = 1 - \frac{\rho_b}{\rho_g} \tag{10}$$

which yields $\theta = 0.72$. This value is in good agreement with the value determined by water loss upon drying at 150 °C ($\theta = 0.74$) after the static experiment.

In the static experiment, the bromide concentration in both reservoirs was 8.5×10^{-4} mol kg_{water}^{-1}. The leaching experiment yielded a bromide concentration value of 6.3×10^{-4} mol kg_{water}^{-1} in the clay plug. Based on these measurements, the bromide accessible (or effective) porosity equals 74% of the total porosity, i.e., $\theta_{e,Br} = 0.55$.

3.1.3. Specific surface charge and mean pore size

The total specific area of montmorillonite layers is $a_s = 770$ m^2 g^{-1} (Bourg et al., 2006; Tournassat and Appelo, 2011). The reported cation exchange capacity of SWy-2 montmorillonite is on the order of 0.85–0.9 mol_c kg^{-1} (Duc et al., 2006; Tertre et al., 2011). Hence, it follows that the surface charge density is about $\sigma_0 = -0.11$ C m^{-2}.

If the pores are assumed to be slit-shaped and residual impurities (non-clay grains) are neglected, the average pore width h_{pore} can be calculated from the relation (Tournassat and Appelo, 2011; Holmboe et al., 2012):

$$h_{pore} = \frac{2 \cdot \theta}{\rho_b a_s} \tag{11}$$

which yields a value of about 24 Å.

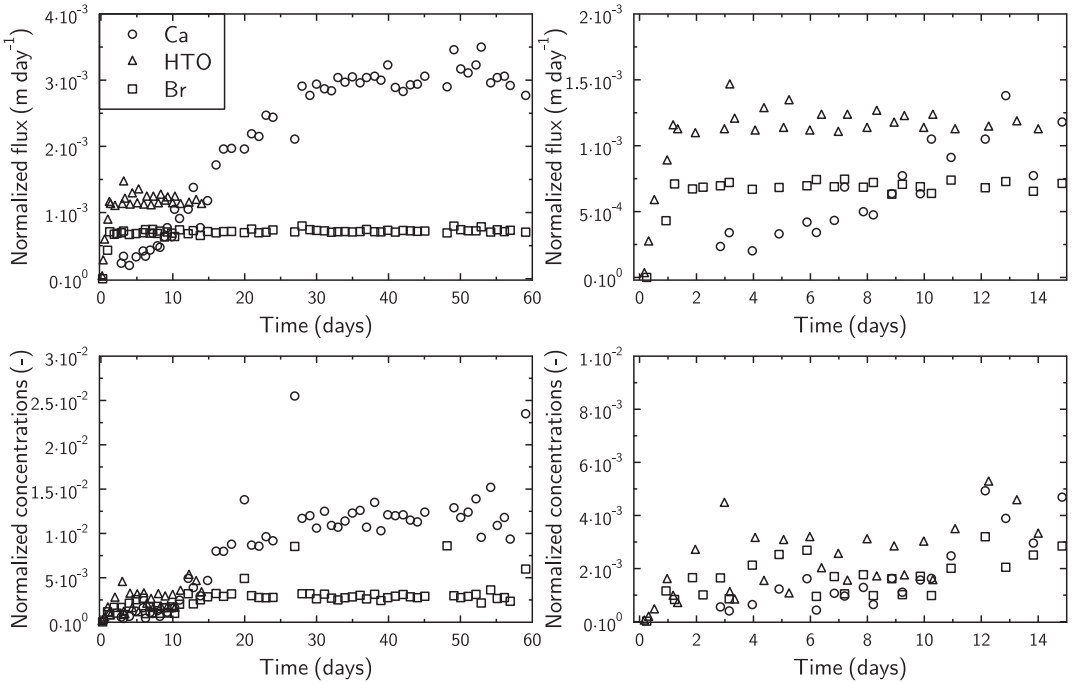


Fig. 3. *Top:* Comparison of normalized mass flux densities as a function of time for Ca (circles), HTO (triangles), and Br (squares). *Bottom:* Comparison of normalized concentrations (same symbols). Right figures show the results for the first 15 days of the diffusion experiments.

3.2. Multi-component transport modeling with simple Fickian diffusion models (Eq. (2))

3.2.1. Diffusion coefficients

3.2.1.1. HTO. In through-diffusion experiments such as those carried out in the present study, the effective diffusion coefficient D_e determines the steady-state flux, whereas the ratio D_e/α determines the duration of the initial transient-state regime. Our steady-state diffusion data yield $D_{e,HTO} = 7.3 \times 10^{-11}$ m^2 s^{-1} based on Eq. (2), in agreement with previous values obtained under similar conditions of salinity and compaction (Tachi and Yotsuji, 2014). The transient-state period in our experiments was too brief to precisely quantify α. However, previous studies indicate that $\alpha = \theta$ in the case of water diffusion in water-saturated bentonite. The model prediction with $D_{e,HTO} = 7.3 \times 10^{-11}$ m^2 s^{-1} and $\alpha = \theta = 0.72$ is consistent with our experimental results (Fig. 4).

According to Eq. (4), the model prediction in Fig. 4 implies that $1/G_{HTO} = 0.047$ if $\theta = 0.72$. [We note, in passing that the calculated value of $1/G_{HTO}$ depends on the value selected for $D_{0,HTO}$, which is not provided in the PHREEQC database. Mills (1973) reported a value of 2.24×10^{-9} m^2 s^{-1} for the diffusion of HTO in H_2O at 298 K. However, other D values used in PHREEQC are based on the compilation of Li and Gregory (1974), in which $D_{0,HTO} = 2.13 \times 10^{-9}$ m^2 s^{-1} at 298 K, as measured by Simpson and Carr (1958). For consistency with our PHREEQC calculations, our other calculations reported hereafter are based on a value of $D_{0,HTO} = 2.13 \times 10^{-9}$ m^2 s^{-1}.] An equally good fit can be obtained with lower or higher porosity values and corresponding lower and higher values for G_{HTO}, because the value of α is not precisely constrained by our experimental data. Therefore, the precision of our fitted G-value is inherently limited by the precision of our porosity estimate. The good agreement between our two θ values ($\theta = 0.72$ based on the dry bulk density in our diffusion experiments; $\theta = 0.74$ based on the water content in our static experiments) suggests that the precision of our fitted G_{HTO} value is on the order of 3%.

3.2.1.2. Bromide. For Br, application of Eq. (2) to our diffusion results yields $D_{e,Br} = 4.4 \times 10^{-11}$ m^2 s^{-1}, a value larger than that obtained by Tachi et al. (2014) but consistent with other studies (Molera et al., 2003; Van Loon et al., 2007). As in the case of HTO, the transient-state period in our experiments was too short to precisely constrain α. However, our static experiments (Section 3.1.2) indicate that $\alpha = \theta_{e,Br} = 0.55$ under the conditions of our diffusion experiments. Model predictions calculated with Eq. (2) with $\alpha = 0.55$ and $D_{e,Br} = 4.4 \times 10^{-11}$ m^2 s^{-1} are consistent with our diffusion results, as shown in Fig. 5. According to Eq. (6) and based on a self-diffusion coefficient for Br^- of 2×10^{-9} m^2 s^{-1} (Li and Gregory, 1974), these values imply that $1/G_{Br} = 0.040$. Hence, the geometric factor associated with Br^- diffusion is either identical or slightly higher than in the case of HTO, in agreement with other studies of water and anion diffusion (Glaus et al., 2010).

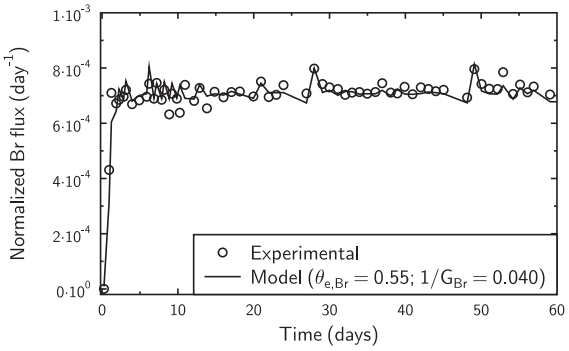


Fig. 5. Br mass flux density as a function of time. *Open circles:* Experimental data. *Full line:* Simple Fickian model with $\alpha = 0.55$ and $D_{e,Br} = 4.4 \times 10^{-11}$ m^2 s^{-1}.

3.2.1.3. Calcium. For Ca^{2+}, a good fit to our diffusion results based on Eq. (2) was obtained with fitted values of $D_{e,Ca} = 2.06 \times 10^{-10}$ m^2 s^{-1} and $\alpha = 63$ (Fig. 6). Based on Eq. (3) and $\rho_b = 0.79$ kg dm^{-3}, this corresponds to a K_D value of ~79 dm^3 kg^{-1}. If we apply Eq. (4) with $\theta = 0.72$ and $D_{0,Ca} = 7.93 \times 10^{-10}$ m^2 s^{-1}, our calculated $D_{e,Ca}$ value yields $1/G_{Ca} = 0.36$. The value of $1/G_{Ca}$ is an order of magnitude higher than $1/G_{Br}$ and $1/G_{HTO}$, indicating that Ca diffusion is enhanced by a factor of ten compared to the diffusion of HTO or Br.

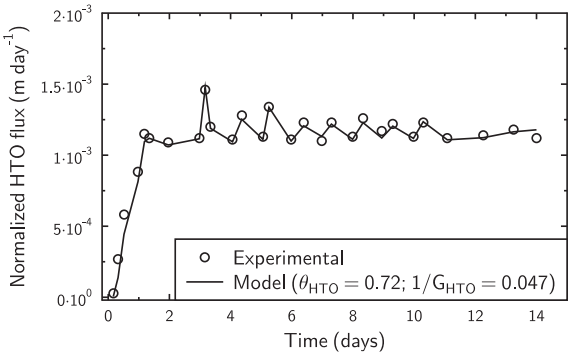


Fig. 4. HTO mass flux density as a function of time. *Open circles:* Experimental data. *Full line:* Simple Fickian model with $\alpha = 0.72$ and $D_{e,HTO} = 7.3 \times 10^{-11}$ m^2 s^{-1}.

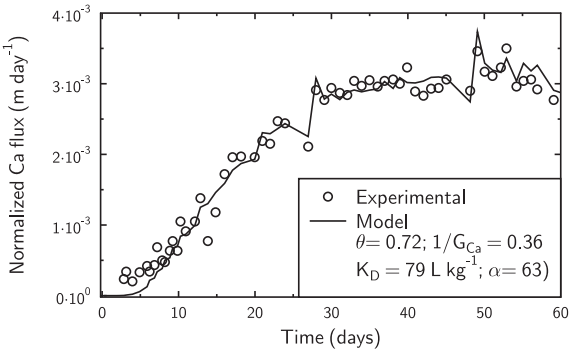


Fig. 6. Ca mass flux density as a function of time. *Open circles:* Experimental data. *Full line:* Simple Fickian model with $\alpha = 63$ and $D_{e,Ca} = 2.06 \times 10^{-10}$ m^2 s^{-1}.

Previous studies indicate that the cause of the rapid diffusion of Ca^{2+} may be more accurately represented using Eq. (7) (without making any assumptions about the microscopic scale basis of the "surface diffusion" coefficient D_s). If we apply Eq. (7), the $D_{e,Ca}$ value used to obtain the model prediction in Fig. 6 is consistent with $1/G_{Ca} = 1/G_{HTO} = 0.047$ with a fitted value of $D_{s,Ca} = 2.82 \times 10^{-12}$ m^2 s^{-1}. If we interpret this value with the relation $D_s = \mu_s D_0/G$, where μ_s is the relative mobility of adsorbed cations (Gimmi and Kosakowski, 2011), our calculated values of $1/G_{Ca}$ and $D_{s,Ca}$ yield $\mu_s = 0.076$. For comparison, Gimmi and Kosakowski (2011) reported $\mu_s \sim 0.1$ for Ca^{2+} based on their compilation of previous studies of diffusion in clayey media. In short, our experimental results are consistent with previous data suggesting that adsorbed Ca^{2+} ions diffuse, on average, roughly 90% slower than "free" (non-adsorbed) Ca^{2+} ions, after accounting for tortuosity.

3.2.2. Lessons learned from simple Fickian models

The present work demonstrates the ability of reactive transport modeling to reduce the uncertainty of calculated transport parameters by identifying the cause of data fluctuation, while taking into account the complex geometry of the experimental system (clay, filters, dead-volumes) and the timing of sampling events. Figs. 4 and 5 clearly show that the fluctuations in the measured mass fluxes in our experiments are primarily due to the sampling procedure and not to other factors such as analytical uncertainties, even though solute concentrations in the low concentration reservoirs were never greater than 2% of the concentration in the high concentration reservoir.

3.3. Molecular dynamics simulations

3.3.1. Average density profiles for water and ions

Molecular dynamics simulations were carried out to examine adsorption and diffusion of water, Br^-, and Ca^{2+} at the scale of an individual pore in conditions that mimic the solid–water ratio and aqueous geochemistry of our diffusion experiments (Fig. 2). Simulation predictions of the average density of ions and water as a function of distance from the clay mineral surface are shown in Fig. 7. Despite significant methodological differences, our simulation results are broadly consistent with those obtained in our previous study focusing on Na–Ca–Cl solutions at higher salinities (0.3–1.8 mol$_c$ dm^{-3}) in 6-nm-wide clay interlayer nanopores (Bourg and Sposito, 2011). Our MD simulations predict the existence of three ordered water layers at $z = 6.1$, 9.5, and 12.4 Å (where $z = 0$ is the mid-plane of the clay mineral particle). The distance between the water density peaks is close to the diameter of a water molecule, indicating that the water layering originates primarily from steric packing at the clay mineral–water interface.

Ion density profiles show that Na^+ and Ca^{2+} are attracted to, and Cl^- and Br^- are repulsed from, the vicinity of the clay mineral surface, as expected from the negative structural charge of the clay mineral layer. For all four ionic species, the density profiles show two peaks near the clay mineral surface: a first peak at $z = (7.65 \pm 0.1)$ Å (for all four ions) and a second peak at $z = (9.95 \pm 0.1)$ Å (for cations) or (10.35 ± 0.1) Å (for anions). The coincidence of the cation and anion density peaks suggests that peak positions may be determined by solvent structure effects such as ion solvation or water density layering. In the context of the well-known triple-layer model (Davis et al., 1978), the cation density peaks reflect adsorption as outer-sphere surface complexes (OSSC) and in the diffuse ion swarm (DIS). The Stern layer contains 37–49% of Na^+ ions and 58–72% of Ca^{2+} ions and screens 39–51% of the surface charge, depending on whether the outer boundary of the Stern layer is identified with the DIS peak or with the density minimum between the OSSC and DIS peak.

Average ion concentrations in the mid-plane of the nanopore (Table 1) show that water in the mid-plane contains significantly more moles of cationic charge ($q_+ = 0.366$ mol$_c$ dm^{-3}) than moles of anionic charge ($q_- = 0.048$ mol$_c$ dm^{-3}). This indicates that the EDLs formed on the two clay mineral surfaces overlap in the center of the nanopore, a phenomenon that strongly influences clay swelling mechanics (Gonçalvès et al., 2007) and ionic mass fluxes in clayey media (Kemper and Rollins, 1966; Neuzil and Provost, 2009).

3.3.2. Composition of bulk liquid water in equilibrium with the simulated nanopore

We can estimate the composition of a fictitious bulk liquid water reservoir in equilibrium with our nanopore in three ways. A first approach consists in applying a Boltzmann relation between concentrations *at the interlayer mid-plane* ($C_{i,\text{mid-plane}}$) and in the bulk solution ($C_{i,\text{bulk}}$ in mol dm^{-3}):

$$C_{i,\text{mid-plane}} = C_{i,\text{bulk}} e^{\frac{-z_i F \psi_{\text{mid-plane}}}{RT}} \tag{12}$$

along with a charge-balance relation in the fictitious bulk aqueous solution:

$$\sum_i z_i C_{i,\text{bulk}} = 0 \tag{13}$$

where z_i is the valence of the ion i of interest, F is the Faraday constant (96485 C mol^{-1}), T is absolute temperature (K), R the gas constant (8.314 J mol^{-1} K^{-1}), and $\psi_{\text{mid-plane}}$ is the electrostatic potential at the mid-plane of the nanopore (V).

A second approach consists in applying Eq. (13) along with a Boltzmann relation between the *average concentrations in the entire nanopore* ($C_{i,\text{pore}}$) and the fictitious solution:

$$C_{i,\text{pore}} = C_{i,\text{bulk}} e^{\frac{-z_i F \psi_{\text{pore}}}{RT}} \tag{14}$$

where ψ_{pore} is an effective "mean electrostatic potential" in the nanopore (V). This approach corresponds to the one used in the LRC and BK models (Fig. 1).

A third approach consists in solving the full Poisson–Boltzmann (PB) equation numerically while adjusting the chemical composition of the fictitious bulk solution to match the MD concentration profiles (Fig. 8; Jardat et al., 2009). For this calculation, the surface charge density was set to -0.114 C m^{-2}. Furthermore, a distance of closest

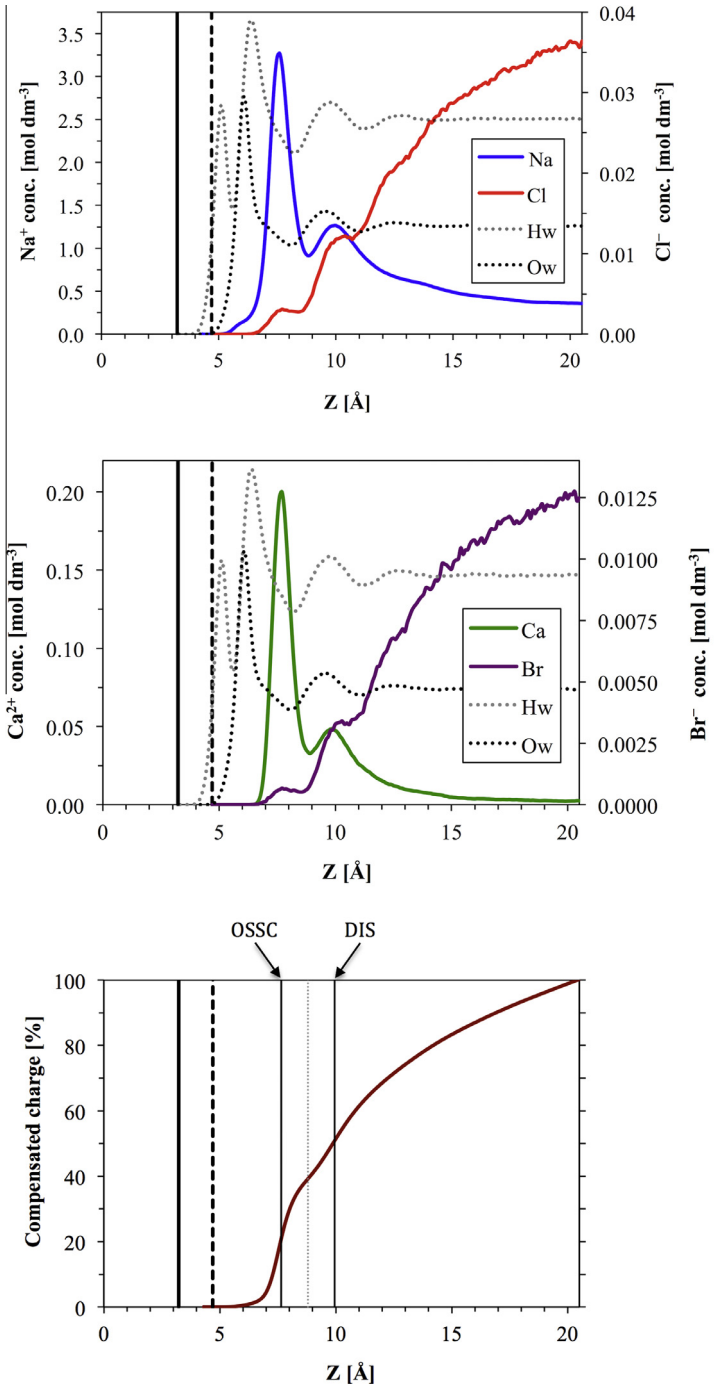


Fig. 7. Molecular dynamics simulation predictions of the average density profiles of water and ions as a function of distance in the direction normal to the clay mineral surface, from the mid-plane of the clay mineral layer ($z = 0$ Å) to the mid-plane of the nanopore ($z = 20.45$ Å). Vertical lines show the location of the plane of surface O atoms (solid line, $z = 3.23$ Å) and the location of the Gibbs dividing surface of liquid water (dashed line, $z = 4.7$ Å). Solid curves show the density profiles of Na^+ and Cl^- (upper figure) and Ca^{2+} and Br^- (middle figure), using a different vertical scale for each ion. Dotted black and gray lines depict the density profiles of water O (Ow) and H (Hw) atoms with an arbitrary vertical scale. The bottom figure shows the cumulative percentage of surface charge compensated by EDL ions as a function of distance from the clay mineral surface, with vertical lines indicating the density peaks of outer-sphere surface complexes (OSSC) and diffuse ion swarm (DIS) cations, respectively.

approach of ions to the clay mineral surface (equal to 2.85 Å, if the location of the clay mineral–water interface is identified with the Gibbs dividing surface of water) was applied to reproduce the position of the first adsorption peak ($z = 7.65 \pm 0.1$ Å), which is the same for all ions. Cation concentrations in the fictitious bulk solution were

Table 1
Molecular dynamics simulation predictions of the average ion concentration in the entire pore ($C_{i,\text{pore}}$) and in the mid-plane of the pore ($C_{i,\text{mid-plane}}$). Ion concentrations in a fictitious bulk water reservoir ($C_{i,\text{bulk}}$) in equilibrium with the pore were calculated using Eqs. (12) and (14), or the Poisson–Boltzmann equation.

Row No.		Br	Cl	Ca	Na
			MD simulation prediction		
1	$C_{i,\text{pore}}$ (mol dm^{-3})	$6.2\cdot10^{-3}$	$1.9\cdot10^{-2}$	$2.5\cdot10^{-2}$	$7.2\cdot10^{-1}$
2	$C_{i,\text{mid-plane}}$ (mol dm^{-3})	$1.3\cdot10^{-2}$	$3.6\cdot10^{-2}$	$2.4\cdot10^{-3}$	$3.6\cdot10^{-1}$
			Eq. (12)		
3	$C_{i,\text{bulk}}$ (mol dm^{-3})	$3.4\cdot10^{-2}$	$9.8\cdot10^{-2}$	$3.2\cdot10^{-4}$	$1.3\cdot10^{-1}$
			Eq. (14)		
4	$C_{i,\text{bulk}}$ (mol dm^{-3})	$3.4\cdot10^{-2}$	$1.0\cdot10^{-1}$	$8.4\cdot10^{-4}$	$1.3\cdot10^{-1}$
			Poisson–Boltzmann equation		
5	$C_{i,\text{pore}}$ (mol dm^{-3})*	$5.7\cdot10^{-3}$	$1.7\cdot10^{-2}$	$1.9\cdot10^{-2}$	$6.5\cdot10^{-1}$
6	$C_{i,\text{bulk}}$ (mol dm^{-3})	$3.4\cdot10^{-2}$	$1.0\cdot10^{-1}$	$3.5\cdot10^{-4}$	$1.4\cdot10^{-1}$
			Adsorption or negative adsorption		
7	m_i (mol kg^{-1})**	$-3.3\cdot10^{-2}$	$-1.0\cdot10^{-1}$	$2.9\cdot10^{-2}$	$6.9\cdot10^{-1}$
8	θ_e/θ (–)**	0.18	0.18	n.a.	n.a.
9	$K_{D,i}$ (dm^3 kg^{-1})**	n.a.	n.a.	83	5.1

* Normalized to the total pore size.
** Calculated using values from rows 1 and 6, $M = 0.84\ \text{kg}_{\text{clay}}\ \text{kg}_{\text{water}}^{-1}$, and Eqs. (15)–(17). Similar values are obtained by combining our MD simulation predictions and the $C_{i,\text{bulk}}$ values calculated with Eq. (12).

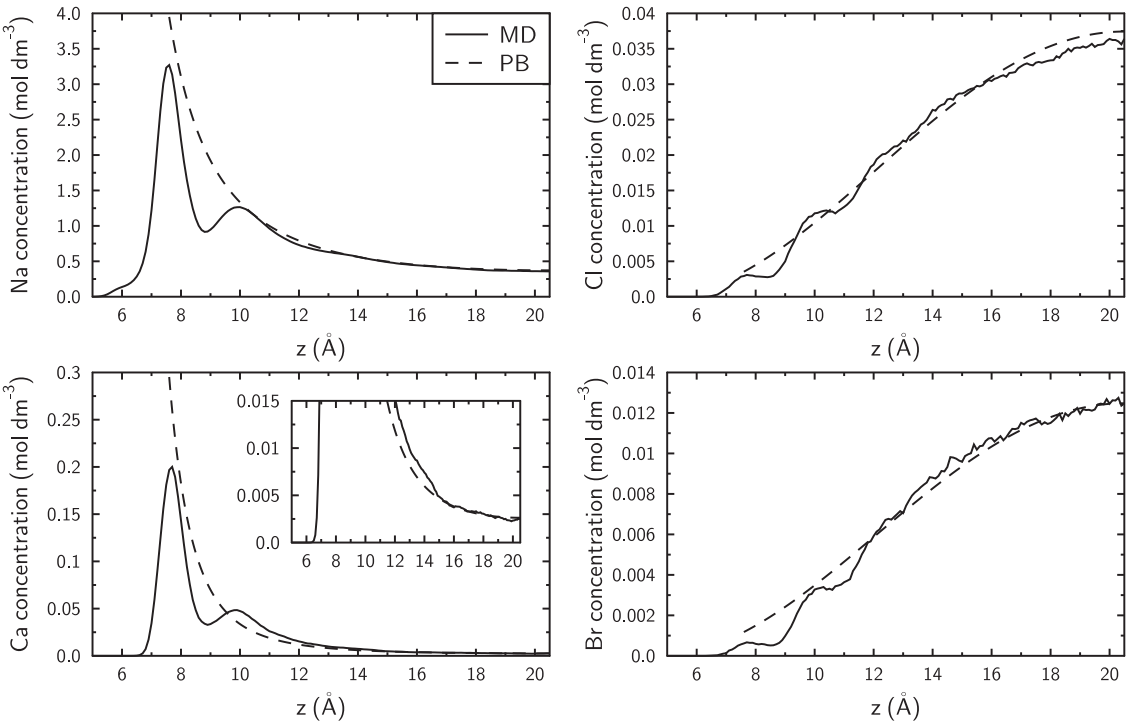


Fig. 8. Cation and anion density profiles as a function of distance from the clay mineral surface: MD simulation results (full lines) and Poisson–Boltzmann model calculation (dashed lines).

adjusted to match the MD concentration profiles. Anion concentrations in the fictitious reservoir are constrained by Eq. (13) and the relation $C_{\text{Cl,bulk}} = 3 \times C_{\text{Br,bulk}}$. This approach is analogous to the one used in the GRR and TY models (Fig. 1), except that these models assume that the distance of closest approach of ions to the clay mineral surface is 0 Å (versus 2.85 Å in our MD simulations).

The excellent agreement for anion profiles between MD calculations and PB predictions justifies the use of the PB equation (without a Stern layer and with a distance of

closest approach of ions to the clay mineral surface equal to 2.85 Å) to estimate the anion accessible porosity in pores of similar size, and for similar ionic strengths and solution compositions. A reasonable agreement between MD results and PB model predictions was also found for the mean concentrations of cations in the pore (23% difference for Ca^{2+}, and 9% difference for Na^{+}). The model based on a Boltzmann factor between the mid-plane of the pore and the fictitious bulk water reservoir (Eq. (12)) gives essentially the same results as the full solution to the PB equation. The model based on a Boltzmann factor between the average pore fluid concentrations and the fictitious bulk water reservoir (Eq. (14), the mean potential model used in the LRC and BK models, Fig. 1) predicts similar concentrations for monovalent ions but it underestimates the ratio $C_{i,\mathrm{pore}}/C_{i,\mathrm{bulk}}$ by a factor of about 2.5 in the case of Ca^{2+}.

3.3.3. Molecular dynamics simulation predictions for anion-accessible porosities, K_D values, and pore scale diffusion coefficients

The values of $C_{i,\mathrm{pore}}$ and $C_{i,\mathrm{bulk}}$ in Table 1 allow us to quantify several ion adsorption (or negative adsorption) coefficients at the nanopore scale. The quantity of adsorbed solute per mass of clay, m_i, can be calculated according to the relation:

$$m_i = \frac{C_{i,\mathrm{pore}} - C_{i,\mathrm{bulk}}}{M} \tag{15}$$

where M is the mass of clay per volume of pore water. For this purpose, the value of M ($M = 0.84\ \mathrm{kg_{clay}\ kg_{water}^{-1}}$) was calculated as the ratio of the dry bulk density used in MD simulations ($0.65\ \mathrm{kg_{clay}\ dm^{-3}}$, Section 3.3) over the mass/volume of water [$(1–0.65)/2.84 = 0.77\ \mathrm{kg_{water}\ dm^{-3}}$], while using a clay mineral layer density value of $2.84\ \mathrm{kg\ dm^{-3}}$. The m_i values given in Table 1 were calculated using the $C_{i,\mathrm{pore}}$ values from MD predictions (row 1, Table 1) and $C_{i,\mathrm{bulk}}$ values obtained from the resolution of the PB equation (row 6, Table 1), which are consistent with our MD simulation results.

Alternatively, adsorption can be expressed as a relative anion-accessible porosity (θ_e/θ) in the case of anions:

$$\frac{\theta_e}{\theta} = \frac{C_{i,\mathrm{pore}}}{C_{i,\mathrm{bulk}}} \tag{16}$$

or as a linear adsorption coefficient ($K_{D,i}$) in the case of cations:

$$K_{D,i} = \frac{m_i}{C_{i,\mathrm{bulk}}} \tag{17}$$

Predicted $K_{D,i}$ values for Na^{+} and Ca^{2+} in our nanopore are consistent with macroscopic scale experimental values reported at similar conditions (Molera and Eriksen, 2002; Wang and Liu, 2004; Tachi and Yotsuji, 2014; Bourg and Tournassat, 2015). However, our predicted value of the relative anion-accessible porosity (θ_e/θ) in our nanopore is much lower than the values obtained in our experiments (Section 3.1.2) or in other experimental studies at similar conditions of salinity and dry bulk density (Molera et al., 2003; Tachi and Yotsuji, 2014; Bourg and Tournassat, 2015).

Molecular dynamics simulation predictions of the diffusion coefficients of water and ions in bulk liquid water (D_{bulk}) and in our clay interlayer nanopore (D_{pore}), reported in Table 2, indicate that all species diffuse more slowly in the nanopore than in bulk liquid water. The influence of confinement, quantified by the factor $q_{\mathrm{nano}} = D_{\mathrm{pore}}/D_{\mathrm{bulk}}$, is essentially identical for all species except Ca^{2+} (Table 2). This difference arises from the fact that calcium is strongly concentrated near the clay mineral surface (even more strongly than Na^{+}), where water and solutes tend to diffuse more slowly. Simulation predictions of the self-diffusion coefficient of water O atoms as a function of distance from the surface (Fig. 9) indicate that in the region between the first and second water layers, where a significant fraction of the cations are adsorbed as OSSC, water diffuses roughly 33% more slowly than bulk liquid water.

4. MODELING AND DISCUSSION

The pore scale diffusion models compiled in Fig. 1 were tested for their ability to reproduce our macroscopic scale experimental results while also being in agreement with our MD simulation results. In the following, we present a comparison of the pore scale models with macroscopic and molecular scale anion exclusion results, as well as with HTO, Ca, and Br diffusion results. Our analysis allows us to draw conclusions regarding the accuracy of single and dual porosity conceptual models of diffusion in compacted smectite.

4.1. Comparison of pore scale models with macroscopic and molecular scale anion exclusion results

The LRC, BK, GRR and TY models (Fig. 1) can be qualified as single porosity EDL diffusion models insofar as the presence of bulk-liquid-like (i.e., non-EDL) water is not explicitly considered in these models. Our MD simulation results show that the Poisson–Boltzmann model (used in the GRR and TY models) and the mean potential model (used in the LCR and BK models) can accurately predict mean anion concentrations in individual nanopores. In short, the pore-scale treatments of anion exclusion in the LRC, BK, GRR, and TY models are qualitatively consistent with MD simulation results, except for the fact that these models do not account for the distance of closest approach of ions to the clay mineral–water interface.

In comparison, the AW model differs from the other pore-scale models in Fig. 1 insofar as it allows for the existence of bulk-liquid-like water in the pore space of compacted clay. In the AW model, the pore space of compacted clay is divided into bulk liquid water (occupying a fraction f of the pore space) and DIS water (or, equivalently, EDL water, the Stern layer being modeled as a region of zero thickness). A mean electrostatic model is applied to the DIS water (Appelo et al., 2010), as described in further detail below. Using Br as an example, if DIS water has the same density as bulk liquid water, and if $C_{i,\mathrm{DIS}}$ is the average concentration of species i in the DIS, then it follows that:

Table 2
Molecular dynamics simulation predictions of the average diffusion coefficients of ions and water in the clay nanopores (D_{pore}) and in bulk liquid water (D_{bulk}). Diffusion coefficients were calculated with Eq. (8) using either $n = 2$ and the mean-square displacement in the xy plane (in the case of D_{pore}), or $n = 3$ and the mean-square displacement in xyz space (in the case of D_{bulk}). Values of D_{bulk} are corrected for a well-established artifact of the periodic boundary conditions that causes a simulation cell size dependence of D in MD simulations of bulk fluids; for D_{pore} no correction is needed as shown in our previous study (Holmboe and Bourg, 2014). The last row shows that $q_{nano} = D_{pore}/D_{bulk}$ is <1 for all species (even anions).

	Br	Cl	Ca	Na	H_2O
D_{pore} (10^{-9} m^2 s^{-1})	1.32 ± 0.15	1.22 ± 0.07	0.47 ± 0.04	0.80 ± 0.01	2.05 ± 0.01
D_{bulk} (10^{-9} m^2 s^{-1})	1.58 ± 0.02	1.68 ± 0.08	0.85 ± 0.04	1.08 ± 0.09	2.68 ± 0.03
q_{nano} (–)	0.83 ± 0.09	0.73 ± 0.05	0.55 ± 0.05	0.74 ± 0.06	0.77 ± 0.01

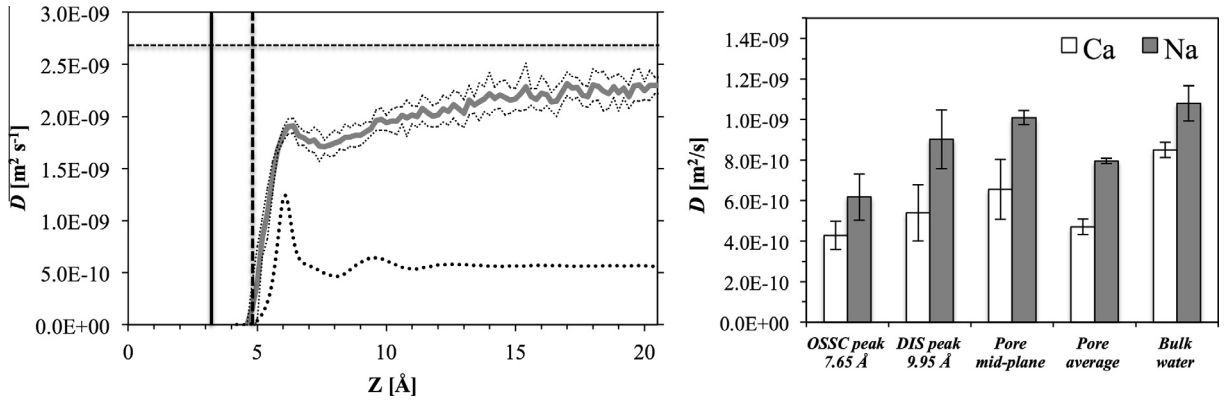


Fig. 9. *Left:* Molecular dynamics simulation prediction of the average diffusion coefficient of water O atoms in the xy-plane as a function of distance from the clay mineral surface, with confidence intervals shown as dashed lines. The self-diffusion coefficient of bulk liquid water is shown by the horizontal dashed line ($D = 2.68{\cdot}10^{-9}$ m^2 s^{-1} for the water model used in our MD simulations, Holmboe and Bourg (2014)); the density profile of water O atoms is shown by the thick dashed line, in arbitrary units. The vertical lines have the same meaning as in Fig. 7. *Right:* Average diffusion coefficients for Na and Ca near the density peaks at $z = 7.65$ Å (OSSC) and 9.95 Å (DIS) and near the pore mid-plane. Average diffusion coefficients in the entire pore and in bulk liquid water are shown for comparison. Note the halved scale compared to the left figure.

$$\theta_{e,Br} \times C_{Br,bulk} = f\theta_{HTO} \times C_{Br,bulk} + (1-f)\theta_{HTO} C_{Br,DIS} \tag{18}$$

In short, the AW model uses f as a fitting parameter that can be constrained by macroscopic anion-exclusion measurements. By comparison, the LRC and BK models make the assumption that the EDL occupies the entire pore space ($f = 0$), while the GRR and TY models use the Poisson–Boltzmann equation to evaluate the thickness of the EDL under the assumption that pore width is uniform.

In the AW model, a mean electrostatic model is used to describe the equilibrium between bulk liquid water and the diffuse ion swarm:

$$C_{Br,DIS} = C_{Br,bulk} \exp\left(\frac{F\psi_{DIS}}{RT}\right) \tag{19}$$

where ψ_{DIS} is the mean electrostatic potential in the diffuse layer. Hence, it follows that:

$$\frac{F\psi_{DIS}}{RT} = \ln\left(\frac{\frac{\theta_{e,Br}}{\theta} - f}{1-f}\right) \tag{20}$$

If we define σ_D as the surface charge that is compensated by ions in the DIS, we can express the charge balance in the diffuse layer as follows:

$$(1-f)\theta\sum_i z_i C_{i,DIS} = -1000\frac{a_s \rho_b \sigma_D}{F} \tag{21}$$

For conditions where Ca is present at trace levels (as in the present study), we obtain:

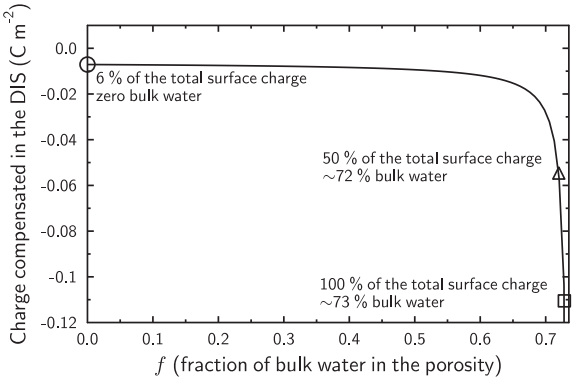


Fig. 10. Relationship between the surface charge compensated in the DIS (full line) and the fraction of the pore space occupied by bulk liquid water (f) according to Eq. (22).

$$\sigma_D = \frac{-2F\theta C_{Na,bulk}(1-f)}{1000 \times a_s \rho_b} \sinh\left(-\ln\left(\frac{\frac{\theta_{e,Br}}{\theta} - f}{1-f}\right)\right) \quad (22)$$

The ratio $\theta_{e,Br}/\theta$ equals 0.74 according to our macroscopic adsorption experiments (Section 3.1.2). All other parameters in Eq. (22) are known and it is, thus, possible to relate the surface charge compensated in the diffuse layer (σ_D) and the mean potential (ψ_{DIS}) to the value of f (Appelo et al., 2010). Fig. 10 demonstrates that, under our experimental conditions, if the Stern layer contributes negligibly to screening the surface charge (as assumed in the BK model), our measured values of $\theta_{e,Br}/\theta$ imply that Br is almost entirely restricted to the bulk liquid water fraction of the pore space ($f \approx \theta_{e,Br}/\theta = 0.74$). In contrast, if the entire pore space is occupied by the DIS, more than 90% of the surface charge must be screened by the Stern layer ($\sigma_D \sim 0.06 \cdot \sigma_0$).

These results indicate that the LRC and BK models (based on a mean electrostatic model with $f = 0$) and, by extension, the GRR and TY models (based on the Poisson–Boltzmann equation, which predicts similar anion-exclusion to the mean electrostatic model with $f = 0$) can only be consistent with our macroscopic experimental results if more than 90% of the charge density σ_0 is screened by the Stern layer. This condition is inconsistent with our MD simulation results, which indicate that concentration profiles of Na, Ca, Br, and Cl are consistent with the Poisson–Boltzmann equation with little or no Stern layer. In short, the LRC, BK, GRR, and TY models cannot be consistent with both our macroscopic scale experimental results and our MD simulation results. Of the pore scale models compiled in Fig. 1, only the AW model has the ability to be consistent with both experimental (showing $\theta_{e,Br}/\theta = 0.74$) and MD simulation results (showing that the Stern layer screens less than 90% of the surface charge).

The AW model, however, only achieves consistency with our results by assuming that $f \approx 0.72$–0.73. This f value would imply that the mean thickness of the EDL (whose fractional porosity value corresponds to $(1-f)\theta$) on the clay mineral surfaces equals,

$$d_D = \frac{(1-f)\theta}{a_s \rho_b \times 10^6} \quad (23)$$

with a resulting value of $d_D \sim 3.4$ Å. This distance, which is approximately equal to the diameter of one water molecule, is too small to be representative of an EDL thickness. This result suggests, firstly, that the value of f in the AW model should be viewed as an overall value of the fraction of DIS water in the entire pore space (not as a value of the fraction of DIS water in each individual nanopore). Secondly, it indicates that the pore space of the compacted clay in our experiments consisted of a mixture of many small pores and a few large pores (with the large pores contributing significantly to the bulk liquid water volume fraction f without contributing much to the average EDL thickness d_D).

4.2. Comparison of pore scale models with macroscopic scale diffusion results

To further test the models in Fig. 1 against our macroscopic scale diffusion results, we implemented the BK, LRC, and AW models in PHREEQC according to the methods described in Appelo and Wersin (2007) and Appelo et al. (2010). Since PHREEQC requires the presence of bulk liquid water in the porous medium, the BK and LRC models were implemented by defining a very small volume of bulk water (0.5% of the total water volume) that does not contribute significantly to the mass balance or diffusive fluxes. The GRR and TY models were not implemented, because PHREEQC does not allow for a solution to the full Poisson–Boltzmann equation.

The BK model assumes that surface charge is completely balanced by DIS ions, while in the LRC model a portion of the charge is screened by cations in the Stern layer. Stern layer adsorption of Na and Ca was taken into account by using the following reactions in the framework of the well-known double layer model (DLM) (Dzombak and Morel, 1990; Parkhurst and Appelo, 1999):

$$Surf^- + Na^+ \rightleftharpoons SurfNa \quad \log K_{Na} \quad (24)$$

$$2Surf^- + Ca^{2+} \rightleftharpoons Surf_2Ca \quad \log K_{Ca} \quad (25)$$

The log K_{Ca} value is constrained by the relative affinities of Ca^{2+} and Na^+ for the surface [$\log K_{Ca} - 2\log K_{Na} \sim 0$–$1$ (Appelo et al., 2010)]. The log K_{Na} value was adjusted to control the extent of surface charge compensation by the Stern layer: a value of −99 results in no surface complexation (BK model) while a value of +1.8 results in a compensation of 90% of the surface charge by Na^+ in the Stern layer (LRC model). The original version of the AW model used $\log K_{Na} = -0.7$, which results in 74% of the surface charge being compensated by the diffuse layer in a 0.1 mol m^{-3} NaCl background electrolyte (Appelo and Wersin, 2007; Appelo et al., 2010). Results from our MD simulations indicate that a log K_{Na} value of 0 may be more appropriate, which results in ~50% of the surface charge being compensated in the diffuse layer (Fig. 7). We note in passing that, according to Fig. 10, at log K_{Na} values smaller than ~1, differences in this parameter have little influence on anion-accessible porosity (or, equivalently, on f), while having a large influence on cation partitioning between bulk water, DIS water, and the Stern layer.

It is possible to adequately fit Ca^{2+} and Br^- diffusion data with both the BK and LRC models using the parameters given in Table 3 (Fig. 11). In the BK model, it is necessary to decrease the mobility of Ca^{2+} by a factor of about 2.5 relative to water. This fitting result is in qualitative (but

Table 3
Diffusion and adsorption parameters for the BK, LRC, and AW models (see Fig. 1 for a description of models).

	BK model	LRC model	AW model
log K_{Na}	−99*	2.1	0
log K_{Ca}	−99*	4.7	0.5
$1/G_{HTO}$	0.047	0.047	0.056
$1/G_{Br}$	0.249	0.040	0.042
$1/G_{Ca}$	0.018	0.207	0.028
f	–	–	0.74
v_{EDL}	–	–	2.2
$\frac{\theta_{e,Br}}{\theta}$	0.1	0.74	0.74

* No adsorption in the Stern layer.

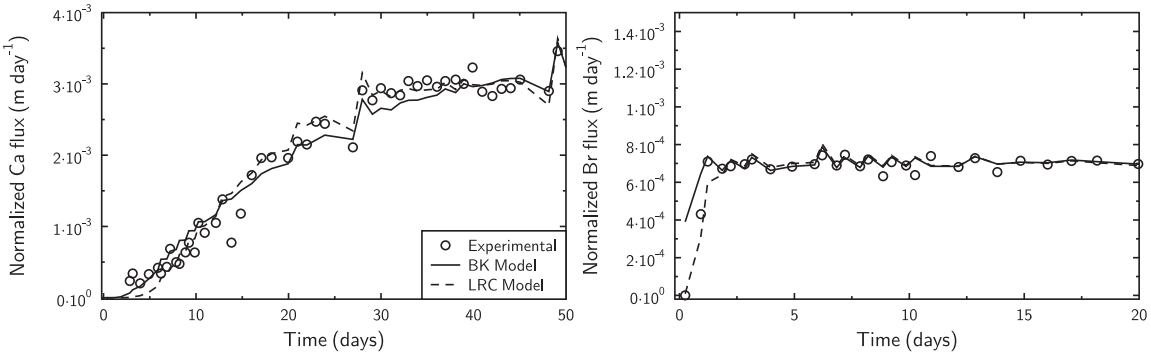


Fig. 11. Ca (left) and Br (right) mass flux densities as a function of time: experimental data (open circles), BK model (full lines), and LRC model (dashed lines). See Fig. 1 for a description of models, and Table 3 for model parameters.

not quantitative) agreement with our MD simulation results, which showed that $q_{nano}(Ca) < q_{nano}(HTO)$ (Table 2). However, a BK model fit also requires an increase in the $1/G$ value for Br^- compared to HTO by a factor of 5.3. Such an adjustment is unsupported by our MD simulations, which showed that $q_{nano}(Br) \cong q_{nano}(HTO)$. In addition, while the Br^- flux at steady state can be adequately reproduced by the BK model, the predicted onset of Br concentration increase occurs too early compared to our experimental results (Fig. 11). Overall, our calculations suggest that the BK model tends to underestimate the Br^- accessible porosity (Table 3), which requires a greater, fitted Br^- mobility in order to match the steady state diffusive flux data.

The LRC model was more successful than the BK model insofar as the simulated and experimentally determined Br accessible porosity values were in good agreement (the $\log K_{Na}$ value was adjusted to obtain this agreement). Furthermore, the relative $1/G$ values of HTO and Br^- were in good agreement with their respective q_{nano} values obtained from MD simulations. However, the fitted $1/G_{Ca}$ value was three times larger than $1/G_{HTO}$, which disagrees with our MD simulation results. As in the case of the Fickian model for Ca^{2+} diffusion (Fig. 6), it is difficult to justify the physical meaning of the very large $1/G$ value of Ca^{2+} (relative to HTO and Br) unless it is assumed that this large $1/G$ value compensates for the assumed immobility of Ca^{2+} surface complexes in the LRC model.

On the AW model, the diffusivity value in the DIS can be varied by defining a parameter v_{DIS} that describes the ratio of the diffusion coefficients for a given species in bulk liquid water and in DIS water. For simplicity, we assume that v_{DIS} has the same value for all species. Consequently, G_{HTO} is constrained by our experimental results according to:

$$\frac{(1-f)}{G_{HTO}} + \frac{f}{v_{DIS} G_{HTO}} = 0.047 \quad (26)$$

The value of G_{Br} is constrained in the same manner. If we neglect the contribution of the diffuse layer to Br^- diffusion, then,

$$\frac{(1-f)}{G_{Br}} \sim 0.040 \times 0.55 \quad (27)$$

Based on this description of diffusion in bulk liquid and DIS water, the AW model (Fig. 12) yields a good fit to the experimental data using the set of parameters given in Table 3. Furthermore, the AW model provides results that are consistent with the measured anion accessible porosity while also satisfying most of the constraints given by molecular dynamics simulations. For instance, the mobility of all species is lower in DIS water than in bulk water. According to our AW model fit, the ratio of diffusion coefficients in DIS water vs. bulk liquid water is $1/v_{DIS} = 0.45$. Hence, the average ratio of HTO diffusion coefficients in the clay pore water (DIS and bulk liquid water) to the diffusion coefficient of HTO in bulk liquid water is equal to $f + 1/v_{DIS} \cdot (1-f) = 0.86$. This value is larger than the value predicted by our MD simulations, $q_{nano} = 0.77 \pm 0.01$ (Table 2). The AW model also predicts that the $1/G$ value of Ca^{2+} is half that of HTO and Br^-, which is in qualitative (but not quantitative) agreement with the somewhat lower value of q_{nano} predicted for Ca relative to Br^- and HTO in our MD simulations (Table 2).

5. SUMMARY

In this study, we tested a variety of pore-scale conceptual models for their ability to reproduce *macroscopic* experimental diffusion data while being in agreement with *molecular scale* results from MD simulations. Based on our findings, single-porosity pore scale models cannot be simultaneously consistent with both macroscopic and molecular scale results. This discrepancy suggests that single porosity models may oversimplify the microstructure of clayey media. Only a model that conceptually divides the pore space of compacted clay into bulk liquid water and diffuse ion swarm (DIS) water (AW model, Fig. 1) was able to simultaneously describe our molecular and macroscopic scale results. Calculations carried out with the AW model suggest that 70% of the pore space of our compacted clay is occupied by bulk liquid water. According to our MD simulation results and Poisson–Boltzmann model calculations, such a large fraction of bulk liquid water cannot exist in our experimental system if the pore size distribution is unimodal. This finding is consistent with direct observations showing that compacted

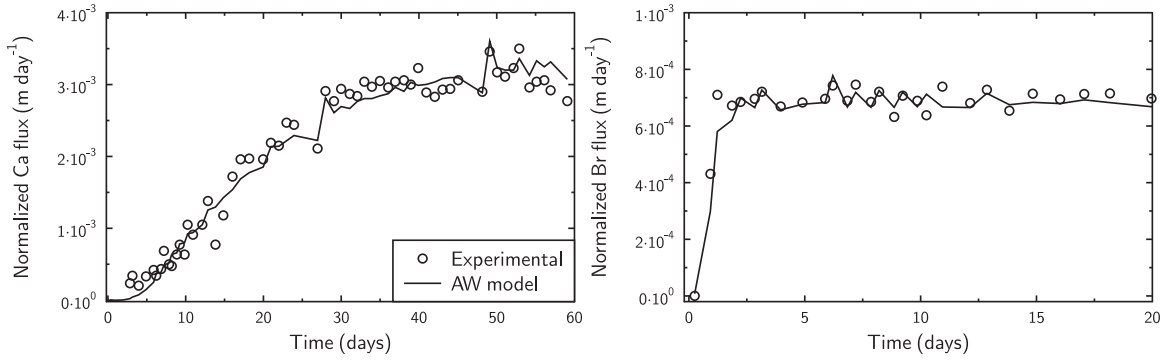


Fig. 12. Ca (left) and Br (right) mass flux densities as a function of time: experimental data (open circles) and AW model (full lines). See Fig. 1 for a description of the model and Table 3 for model parameters.

Na-montmorillonite displays a significant microstructural complexity (Pusch, 2001; Melkior et al., 2009) that can strongly impact anion accessible porosity (Tournassat and Appelo, 2011). Our results, therefore, reveal that a very detailed experimental characterization of pore structure (down to the resolution of the interlayer nanopores) as a function of dry density and electrolyte concentration may be necessary to further constrain models of diffusion in clayey media. As a first step, the existence of relatively large pores in compacted, water-saturated Na-montmorillonite at our experimental conditions (on the order of tens of nanometers and accounting for ~70% of the pore space, despite the significant swelling pressure of the material) should be evaluated.

An alternative explanation for the failure of single porosity models to capture both macroscale and pore scale behaviors could be that these models do not accurately describe adsorption and diffusion at the pore scale. This hypothesis, however, is inconsistent with our findings. The descriptions of adsorption and diffusion used in existing single porosity pore scale models largely agree with our MD simulation results. In particular, our atomistic simulations show that cation adsorption and anion exclusion in individual nanopores are consistent with the Poisson–Boltzmann equation used in the GRR and TY models (but with a distance of closest approach of ions to the clay mineral surface, a feature absent from existing pore scale diffusion models). Our MD simulation results on the adsorption of Na, Cl, and Br (but not Ca) also are consistent with the "mean electrostatic" approximation applied in the AW, LRC, and BK models. Our pore scale simulations further indicate that a Stern layer is not necessary to describe the adsorption of Na^+, Ca^{2+}, Cl^-, and Br^- in Na-montmorillonite (MD simulation results are adequately described by a Poisson–Boltzmann model calculation without a Stern layer). However, if Na^+ and Ca^{2+} outer-sphere surface complexes (OSSC) are conceptually viewed as forming a Stern layer, then this layer screens about 40–50% of the surface charge.

With regard to cation diffusion, our MD simulations clearly show that Na^+ and Ca^{2+} ions adsorbed as OSSC retain a significant mobility. Therefore, a possible future improvement to the conceptual diffusion models discussed here is the introduction of Stern layer diffusion (in addition to diffusion in bulk liquid water and in DIS water). This approach, however, creates the challenge of finding a unique distribution of properties for the three domains (bulk liquid water, DIS water, and Stern layer) that can reproduce macroscopic diffusion data for cations, anions, and neutral species while remaining in agreement with molecular scale information. In this study, we did not attempt to develop such a model, because its parameterization would be under-constrained by currently available data.

Finally, our results demonstrate that reactive transport modeling can improve the accuracy with which diffusion and transport parameters are derived from diffusion experiments, by taking into account the full geometry of the system (clay, filters, dead-volumes) as well as the specific nature of the sampling procedure. In the present study, reactive transport modeling results demonstrated that fluctuations in measured solute mass fluxes were primarily due to the timing of sampling events and not to other factors such as analytical uncertainties.

ACKNOWLEDGEMENTS

This research was supported by the U.S. Department of Energy under Contract DE-AC02-05CH11231 under the auspices of the Used Fuel Disposition program (Office of Nuclear Energy) and the Geosciences program (Office of Science, Office of Basic Energy Sciences) as well as by the French Geologic Survey (BRGM) through the Institut Carnot BRGM. It used resources of the National Energy Research Scientific Computing Center (NERSC), which is supported by the Office of Science of the U.S. Department of Energy under Contract DE-AC02-05CH11231. Financial support to M.H. by the Carl Tryggers Foundation, the Gålö Foundation, and the foundation BLANCEFLOR is gratefully acknowledged. The authors would like to thank Prof. Jonsson and co-workers at the Applied Physical Chemistry, KTH, Sweden, for providing the diffusion cells used in this study.

APPENDIX A. SUPPLEMENTARY DATA

Supplementary data associated with this article can be found, in the online version, at http://dx.doi.org/10.1016/j.gca.2015.12.010.

REFERENCES

Aaqvist J. (1990) Ion-water interaction potentials derived from free energy perturbation simulations. *J. Phys. Chem.* **94**, 8021–8024.

Altmann S. (2008) Geochemical research: a key building block for nuclear waste disposal safety cases. *J. Contam. Hydrol.* **102**, 174–179.

Altmann S., Tournassat C., Goutelard F., Parneix J.-C., Gimmi T. and Maes N. (2012) Diffusion-driven transport in clayrock formations. *Appl. Geochem.* **27**, 463–478.

Andra (2005) Référentiel du comportement des radionucléides et des toxiques chimiques d'un stockage dans le Callovo-Oxfordien jusqu'à l'Homme. Dossier 2005 Argile. Agence Nationale pour la gestion des déchets radioactifs, Châtenay-Malabry, France.

Appelo C. A. J. and Wersin P. (2007) Multicomponent diffusion modeling in clay systems with application to the diffusion of tritium, iodide, and sodium in Opalinus clay. *Environ. Sci. Technol.* **41**, 5002–5007.

Appelo C. A. J., Van Loon L. R. and Wersin P. (2010) Multicomponent diffusion of a suite of tracers (HTO, Cl, Br, I, Na, Sr, Cs) in a single sample of Opalinus clay. *Geochim. Cosmochim. Acta* **74**, 1201–1219.

Bear J. (1972) *Dynamics of Fluids in Porous Media*. Courier Dover Publications.

Berendsen H. J. C., Grigera J. R. and Straatsma T. P. (1987) The missing term in effective pair potentials. *J. Phys. Chem.* **91**, 6269–6271.

Birgersson M. and Karnland O. (2009) Ion equilibrium between montmorillonite interlayer space and an external solution – consequences for diffusional transport. *Geochim. Cosmochim. Acta* **73**, 1908–1923.

Bock H., Dehandschutter B., Martin C. D., Mazurek M., De Haller A., Skoczylas F. and Davy C. (2010) *Self-sealing Fractures in Argillaceous Formations in the Context of Geological Disposal of Radioactive was (No. 6184)*. Nuclear Energy Agency, Organisation for Economic Co-operation and Development.

Bourg I. C. and Sposito G. (2010) Connecting the molecular scale to the continuum scale for diffusion processes in smectite-rich porous media. *Environ. Sci. Technol.* **44**, 2085–2091.

Bourg I. C. and Sposito G. (2011) Molecular dynamics simulations of the electrical double layer on smectite surfaces contacting concentrated mixed electrolyte (NaCl–$CaCl_2$) solutions. *J. Colloid Interface Sci.* **360**, 701–715.

Bourg I. C. and Tournassat C. (2015) Chapter 6 – self-diffusion of water and ions in clay barriers. In *Natural and Engineered Clay Barriers, Developments in Clay Science* (eds. C. Tournassat, C. I. Steefel, I. C. Bourg and F. Bergaya). Elsevier, pp. 71–100.

Bourg I. C., Sposito G. and Bourg A. C. M. (2006) Tracer diffusion in compacted, water-saturated bentonite. *Clays Clay Miner.* **54**, 363–374.

Bradbury M. H. and Baeyens B. (2011) Predictive sorption modelling of Ni(II), Co(II), Eu(IIII), Th(IV) and U(VI) on MX-80 bentonite and Opalinus clay: a "bottom-up" approach. *Appl. Clay Sci.* **52**, 27–33.

Chipera S. J. and Bish D. L. (2001) Baseline studies of the clay minerals society source clays: powder X-ray diffraction analyses. *Clays Clay Miner.* **49**, 398–409.

Churakov S. V. and Gimmi T. (2011) Up-scaling of molecular diffusion coefficients in clays: a two-step approach. *J. Phys. Chem. C* **115**, 6703–6714.

Costanzo P. and Guggenheim S. (2001) Baseline studies of the Clay Minerals Society source clays: preface. *Clays Clay Miner.* **49**, 371.

Cygan R. T., Liang J.-J. and Kalinichev A. G. (2004) Molecular models of hydroxide, oxyhydroxide, and clay phases and the development of a general force field. *J. Phys. Chem. B* **108**, 1255–1266.

Davis J. A., James R. O. and Leckie J. O. (1978) Surface ionization and complexation at the oxide/water interface. I. Computation of electrical double layer properties in simple electrolytes. *J. Colloid Interface Sci.* **63**, 480–499.

Delay J., Vinsot A., Krieguer J.-M., Rebours H. and Armand G. (2007) Making of the underground scientific experimental programme at the Meuse/Haute-Marne underground research laboratory, North Eastern France. *Phys. Chem. Earth Parts A/B/C* **32**, 2–18.

Duc M., Thomas F. and Gaboriaud F. (2006) Coupled chemical processes at clay/electrolyte interface: a batch titration study of Na-montmorillonites. *J. Colloid Interface Sci.* **300**, 616–625.

Dykhuizen R. C. and Casey W. H. (1989) An analysis of solute diffusion in rocks. *Geochim. Cosmochim. Acta* **53**, 2797–2805.

Dzombak D. A. and Morel F. M. M. (1990) *Surface Complexation Modeling-Hydrous Ferric Oxide. New York*.

Englert M., Krall L. and Ewing R. C. (2012) Is nuclear fission a sustainable source of energy?. *MRS Bull.* **37** 417–424.

Ferrage E., Lanson B., Sakharov B. A. and Drits V. A. (2005) Investigation of smectite hydration properties by modeling experimental X-ray diffraction patterns. Part I. Montmorillonite hydration properties. *Am. Mineral.* **90**, 1358–1374.

Gajo A. and Loret B. (2007) The mechanics of active clays circulated by salts, acids and bases. *J. Mech. Phys. Solids* **55**, 1762–1801.

Gimmi T. and Kosakowski G. (2011) How mobile are sorbed cations in clays and clay rocks? *Environ. Sci. Technol.* **45**, 1443–1449.

Glaus M. A., Frick S., Rosse R. and Van Loon L. R. (2010) Comparative study of tracer diffusion of HTO, Na-22(+) and Cl-36(−) in compacted kaolinite, illite and montmorillonite. *Geochim. Cosmochim. Acta* **74**, 1999–2010.

Glaus M. A., Aertsens M., Maes N., Van Laer L. and Van Loon L. R. (2015) Treatment of boundary conditions in through-diffusion: a case study of $^{85}Sr^{2+}$ diffusion in compacted illite. *J. Contam. Hydrol.* **177**, 239–248.

Gonçalvès J., Rousseau-Gueutin P. and Revil A. (2007) Introducing interacting diffuse layers in TLM calculations: a reappraisal of the influence of the pore size on the swelling pressure and the osmotic efficiency of compacted bentonites. *J. Colloid Interface Sci.* **316**, 92–99.

Gonzàlez Sànchez F., Gimmi T., Juranyi F., Van Loon L. and Diamond L. W. (2009) Linking the diffusion of water in compacted clays at two different time scales: tracer through-diffusion and quasielastic neutron scattering. *Environ. Sci. Technol.* **43**, 3487–3493.

Guyonnet D., Touze-Foltz N., Norotte V., Pothier C., Didier G., Gailhanou H., Blanc P. and Warmont F. (2009) Performance-based indicators for controlling geosynthetic clay liners in landfill applications. *Geotext. Geomembr.* **27**, 321–331.

Hockney R. W. and Eastwood J. W. (1988) *Computer Simulation Using Particles*. Hilger, Bristol England and Philadelphia.

Holmboe M. and Bourg I. C. (2014) Molecular dynamics simulations of water and sodium diffusion in smectite interlayer nanopores as a function of pore size and temperature. *J. Phys. Chem. C* **118**, 1001–1013.

Holmboe M., Wold S. and Jonsson M. (2010) Colloid diffusion in compacted bentonite: microstructural constraints. *Clays Clay Miner.* **58**, 532–541.

Holmboe M., Karin Norrfors K., Jonsson M. and Wold S. (2011) Effect of γ-radiation on radionuclide retention in compacted bentonite. *Radiat. Phys. Chem.* **80**, 1371–1377.

Holmboe M., Wold S. and Jonsson M. (2012) Porosity investigation of compacted bentonite using XRD profile modeling. *J. Contam. Hydrol.* **128**, 19–32.

Horseman S. T. and Volckaert G. (1996) Disposal of Radioactive Wastes in Argillaceous Formations. *Geological Society, London, Engineering Geology Special Publications* **11**, 179–191.

Isele-Holder R. E., Mitchell W. and Ismail A. E. (2012) Development and application of a particle–particle particle-mesh Ewald method for dispersion interactions. *J. Chem. Phys.* **137**, 174107.

Jackson M. L. (1975) *Soil Chemical Analysis – Advanced Course*, second ed. Published by the author, University of Wisconsin, Madison, Wisconsin.

Jakob A., Pfingsten W. and Van Loon L. R. (2009) Effects of sorption competition on caesium diffusion through compacted argillaceous rock. *Geochim. Cosmochim. Acta* **73**, 2441–2456.

Jardat M., Dufreche J. F., Marry V., Rotenberg B. and Turq P. (2009) Salt exclusion in charged porous media: a coarse-graining strategy in the case of montmorillonite clays. *Phys. Chem. Chem. Phys.* **11**, 2023–2033.

Jenny H. and Overstreet R. (1939) Surface migration of ions and contact exchange. *J. Phys. Chem.* **43**, 1185–1196.

Jo H. Y., Benson C. H. and Edil T. B. (2006) Rate-limited cation exchange in thin bentonitic barrier layers. *Can. Geotech. J.* **43**, 370–391.

Joseph C., Schmeide K., Sachs S., Brendler V., Geipel G. and Bernhard G. (2011) Sorption of uranium (VI) onto Opalinus clay in the absence and presence of humic acid in Opalinus clay pore water. *Chem. Geol.* **284**, 240–250.

Jougnot D., Revil A. and Leroy P. (2009) Diffusion of ionic tracers in the Callovo-Oxfordian clay–rock using the Donnan equilibrium model and the formation factor. *Geochim. Cosmochim. Acta* **73**, 2712–2726.

Joung I. S. and Cheatham T. E. I. (2009) Molecular dynamics simulations of the dynamic and energetic properties of alkali and halide ions using water-model-specific ion parameters. *J. Phys. Chem. B* **113**, 13279–13290.

Keller L. M., Holzer L., Schuetz P. and Gasser P. (2013) Pore space relevant for gas permeability in Opalinus clay: statistical analysis of homogeneity, percolation, and representative volume element. *J. Geophys. Res.* **118**, 2799–2812.

Kemper W. D. and Rollins J. B. (1966) Osmotic efficiency coefficients across compacted clays. *Soil Sci. Soc. Am. J.* **30**, 529–534.

Kemper W. D., Maasland D. E. L. and Porter L. K. (1964) Mobility of water adjacent to mineral surfaces. *Soil Sci. Soc. Am. J.* **28**, 164–167.

Kerisit S. and Liu C. (2010) Molecular simulation of the diffusion of uranyl carbonate species in aqueous solution. *Geochim. Cosmochim. Acta* **74**, 4937–4952.

Laird D. A. and Shang C. (1997) Relationship between cation exchange selectivity and crystalline swelling in expanding 2:1 phyllosilicates. *Clays Clay Miner.* **45**, 681–689.

Leroy P., Revil A. and Coelho D. (2006) Diffusion of ionic species in bentonite. *J. Colloid Interface Sci.* **296**, 248–255.

Li Y.-H. and Gregory S. (1974) Diffusion of ions in sea water and in deep-sea sediments. *Geochim. Cosmochim. Acta* **38**, 703–714.

Loomer D. B., Scott L., Al T. A., Mayer K. U. and Bea S. (2013) Diffusion–reaction studies in low permeability shale using X-ray radiography with cesium. *Appl. Geochem.* **39**, 49–58.

Marry V., Turq P., Cartailler T. and Levesque D. (2002) Microscopic simulation for structure and dynamics of water and counterions in a monohydrated montmorillonite. *J. Chem. Phys.* **117**, 3454–3463.

Marry V., Rotenberg B. and Turq P. (2008) Structure and dynamics of water at a clay surface from molecular dynamics simulation. *Phys. Chem. Chem. Phys.* **10**, 4802–4813.

Mazurek M., Alt-Epping P., Bath A., Gimmi T., Niklaus Waber H., Buschaert S., Cannière P. D., De Craen M., Gautschi A., Savoye S., Vinsot A., Wemaere I. and Wouters L. (2011) Natural tracer profiles across argillaceous formations. *Appl. Geochem.* **26**, 1035–1064.

Melkior T., Gaucher E. C., Brouard C., Yahiaoui S., Thoby D., Clinard C., Ferrage E., Guyonnet D., Tournassat C. and Coelho D. (2009) Na^+ and HTO diffusion in compacted bentonite: effect of surface chemistry and related texture. *J. Hydrol.* **370**, 9–20.

Mermut A. R. and Cano A. F. (2001) Baseline studies of the clay minerals society source clays: chemical analyses of major elements. *Clays Clay Miner.* **49**, 381–386.

Mills R. (1973) Self-diffusion in normal and heavy-water in range 1–45 degrees. *J. Phys. Chem.* **77**, 685–688.

Molera M. (2002) *On the Sorption and Diffusion of Radionuclides in Bentonite Clay* (Ph.D. thesis). Royal Institute of Technology, Stockholm.

Molera M. and Eriksen T. (2002) Diffusion of $^{22}Na^+$, $^{85}Sr^{2+}$, $^{134}Cs^+$ and $^{57}Co^{2+}$ in bentonite clay compacted to different densities: experiments and modeling. *Radiochim. Acta* **90**, 753–760.

Molera M., Eriksen T. and Jansson M. (2003) Anion diffusion pathways in bentonite clay compacted to different dry densities. *Appl. Clay Sci.* **23**, 69–76.

Montavon G., Guo Z., Tournassat C., Grambow B. and Le Botlan D. (2009) Porosities accessible to HTO and iodide on water-saturated compacted clay materials and relation with the forms of water: a low field proton NMR study. *Geochim. Cosmochim. Acta* **73**, 7290–7302.

Muurinen A., Karnland O. and Lehikoinen J. (2004) Ion concentration caused by an external solution into the porewater of compacted bentonite. *Phys. Chem. Earth Parts A/B/C* **29**, 119–127.

Muurinen A., Karnland O. and Lehikoinen J. (2007) Effect of homogenization on the microstructure and exclusion of chloride in compacted bentonite. *Phys. Chem. Earth Parts A/B/C* **32**, 485–490.

Nadeau P. H. (1985) The physical dimensions of fundamental clay particles. *Clay Miner.* **20**, 499.

Neuzil C. E. (1986) Groundwater flow in low-permeability environments. *Water Resour. Res.* **22**, 1163–1195.

Neuzil C. E. (1994) How permeable are clays and shales? *Water Resour. Res.* **30**, 145–150.

Neuzil C. E. (2013) Can shale safely host US nuclear waste? *EOS Trans. Am. Geophys. Union* **94**, 261–262.

Neuzil C. E. and Provost A. M. (2009) Recent experimental data may point to a greater role for osmotic pressures in the subsurface. *Water Resour. Res.* **45**.

Nye P. H. (1980) Diffusion of ions and uncharged solutes in soils and soil clays. *Adv. Agron.* **31**, 225–272.

Oscarson D. W., Dixon D. A. and Hume H. B. (1996) Mass transport through defected bentonite plugs. *Appl. Clay Sci.* **11**, 127–142.

Pacala S. and Socolow R. (2004) Stabilization wedges: solving the climate problem for the next 50 years with current technologies. *Science* **305**, 968–972.

Parkhurst D. L. and Appelo C. A. J. (1999) *User's guide to PHREEQC (version 2) – a computer program for speciation, batch-reaction, one-dimensional transport, and inverse geochemical calculations (No. Denver, CO. U.S. Geological Survey)*, 312p.

Parkhurst D. L. and Appelo C. A. J. (2013) *Description of Input and Examples for PHREEQC Version 3—A Computer Program for Speciation, Batch-reaction, One-dimensional Transport, and Inverse Geochemical Calculations*.

Plimpton S. (1995) Fast parallel algorithms for short-range molecular dynamics. *J. Comput. Phys.* **117**, 1–19.

Pusch R. (2001) *The Microstructure of MX-80 Clay with Respect to its Bulk Physical Properties under Different Environmental Conditions. SKB, TR-01-08*.

Ryckaert J.-P., Ciccotti G. and Berendsen H. J. C. (1977) Numerical integration of the Cartesian equations of motion of a system with constraints: molecular dynamics of *n*-alkanes. *J. Comput. Phys.* **23**, 327–341.

Sato H. (2008) Thermodynamic model on swelling of bentonite buffer and backfill materials. *Phys. Chem. Earth Parts A/B/C* **33**, S538–S543.

Savoye S., Page J., Puente C., Imbert C. and Coelho D. (2010) New experimental approach for studying diffusion through an intact and unsaturated medium: a case study with Callovo-Oxfordian argillite. *Environ. Sci. Technol.* **44**, 3698–3704.

Savoye S., Goutelard F., Beaucaire C., Charles Y., Fayette A., Herbette M., Larabi Y. and Coelho D. (2011) Effect of temperature on the containment properties of argillaceous rocks: the case study of Callovo-Oxfordian claystones. *J. Contam. Hydrol.* **125**, 102–112.

Shackelford C. D. and Moore S. M. (2013) Fickian diffusion of radionuclides for engineered containment barriers: diffusion coefficients, porosities, and complicating issues. *Eng. Geol.* **152**, 133–147.

Simpson J. H. and Carr H. Y. (1958) Diffusion and nuclear spin relaxation in water. *Phys. Rev.* **111**, 1201.

SKB (2011) *Long-term safety for the final repository for spent nuclear fuel at Forsmark*, SKB-TR-11-01.

Sposito G. (1992) The diffuse-ion swarm near smectite particles suspended in 1:1 electrolyte solutions: modified Gouy-Chapman theory and quasicrystal formation. In *Clay Water Interface and its Rheological Implications* (eds. N. Güven and R. M. Pollastro), pp. 127–156. Main Report of the SR-Site Project. Clay minerals society.

Sposito G. (2004) *The Surface Chemistry of Natural Particles*. Oxford University Press, New York.

Sposito G., Skipper N. T., Sutton R., Park S. and Soper A. K. (1999) Surface geochemistry of the clay minerals. *Proc. Natl. Acad. Sci. U.S.A.* **96**, 3358–3364.

Swift A. M., Anovitz L. M., Sheets J. M., Cole D. R., Welch S. A. and Rother G. (2014) Relationship between mineralogy and porosity in seals relevant to geologic CO_2 sequestration. *Environ. Geosci.* **21**, 39–57.

Tachi Y. and Yotsuji K. (2014) Diffusion and sorption of Cs^+, Na^+, I^- and HTO in compacted sodium montmorillonite as a function of porewater salinity: integrated sorption and diffusion model. *Geochim. Cosmochim. Acta* **132**, 75–93.

Tachi Y., Yotsuji K., Suyama T. and Ochs M. (2014) Integrated sorption and diffusion model for bentonite. Part 2. Porewater chemistry, sorption and diffusion modeling in compacted systems. *J. Nucl. Sci. Technol.* **51**, 1–14.

Tertre E., Pret D. and Ferrage E. (2011) Influence of the ionic strength and solid/solution ratio on Ca(II)-for-Na+ exchange on montmorillonite. Part 1. Chemical measurements, thermodynamic modeling and potential implications for trace elements geochemistry. *J. Colloid Interface Sci.* **353**, 248–256.

Tournassat C. and Appelo C. A. J. (2011) Modelling approaches for anion-exclusion in compacted Na-bentonite. *Geochim. Cosmochim. Acta* **75**, 3698–3710.

Tournassat C., Neaman A., Villiéras F., Bosbach D. and Charlet L. (2003) Nanomorphology of montmorillonite particles: estimation of the clay edge sorption site density by low-pressure gas adsorption and AFM observations. *Am. Mineral.* **88**, 1989–1995.

Tournassat C., Chapron Y., Leroy P. and Boulahya F. (2009) Comparison of molecular dynamics simulations with triple layer and modified Gouy-Chapman models in a 0.1 M NaCl – montmorillonite system. *J. Colloid Interface Sci.* **339**, 533–541.

Van Loon L. R., Soler J. M. and Bradbury M. H. (2003a) Diffusion of HTO, $^{36}Cl^-$ and $^{125}I^-$ in Opalinus clay samples from Mont Terri: effect of confining pressure. *J. Contam. Hydrol.* **61**, 73–83.

Van Loon L. R., Soler J. M., Jakob A. and Bradbury M. H. (2003b) Effect of confining pressure on the diffusion of HTO, $^{36}Cl^-$ and $^{125}I^-$ in a layered argillaceous rock (Opalinus clay): diffusion perpendicular to the fabric. *Appl. Geochem.* **18**, 1653–1662.

Van Loon L. R., Glaus M. A. and Müller W. (2007) Anion exclusion effects in compacted bentonites: towards a better understanding of anion diffusion. *Appl. Geochem.* **22**, 2536–2552.

Van Schaik J. and Kemper W. (1966) Chloride diffusion in clay–water systems. *Soil Sci. Soc. Am. J.* **30**, 22–25.

Van Schaik J., Kemper W. and Olsen S. (1966) Contribution of adsorbed cations to diffusion in clay–water systems. *Soil Sci. Soc. Am. J.* **30**, 17–22.

Wang X. and Liu X. (2004) Effect of pH and concentration on the diffusion of radiostrontium in compacted bentonite—a capillary experimental study. *Appl. Radiat. Isot.* **61**, 1413–1418.

Wang Q., Tang A. M., Cui Y.-J., Barnichon J.-D. and Ye W.-M. (2013) Investigation of the hydro-mechanical behaviour of compacted bentonite/sand mixture based on the BExM model. *Comput. Geotech.* **54**, 46–52.

Wersin P., Curti E. and Appelo C. A. J. (2004) Modelling bentonite–water interactions at high solid/liquid ratios: swelling and diffuse double layer effects. *Appl. Clay Sci.* **26**, 249–257.

Yokoyama S., Kuroda M. and Sato T. (2005) Atomic force microscopy study of montmorillonite dissolution under highly alkaline conditions. *Clays Clay Miner.* **53**, 147–154.

Zachara J. M. and Smith S. C. (1994) Edge complexation reactions of cadmium on specimen and soil-derived smectite. *Soil Sci. Soc. Am. J.* **58**, 762–769.

Associate editor: Annie B. Kersting